

# Perfect control of photoelectron anisotropy for randomly oriented ensembles of molecules by XUV REMPI and polarization shaping

Cite as: J. Chem. Phys. **151**, 074106 (2019); <https://doi.org/10.1063/1.5111362>

Submitted: 25 May 2019 . Accepted: 16 July 2019 . Published Online: 15 August 2019

R. Esteban Goetz , Christiane P. Koch , and Loren Greenman

## COLLECTIONS

Note: This paper is part of the JCP special collection on Ultrafast Spectroscopy and Diffraction from XUV to X-ray.

 This paper was selected as Featured



View Online



Export Citation



CrossMark

## ARTICLES YOU MAY BE INTERESTED IN

[Angular dependence of strong field ionization of N<sub>2</sub> by time-dependent configuration interaction using density functional theory and the Tamm-Dancoff approximation](#)

The Journal of Chemical Physics **151**, 054102 (2019); <https://doi.org/10.1063/1.5108846>

[Platinum, gold, and silver standards of intermolecular interaction energy calculations](#)

The Journal of Chemical Physics **151**, 070901 (2019); <https://doi.org/10.1063/1.5116151>

[Coupling of electronic and nuclear motion in a negative ion resonance: Experimental and theoretical study of benzene](#)

The Journal of Chemical Physics **151**, 064119 (2019); <https://doi.org/10.1063/1.5110677>

The Journal  
of Chemical Physics

Submit Today

The Emerging Investigators Special Collection and Awards  
Recognizing the excellent work of early career researchers!



# Perfect control of photoelectron anisotropy for randomly oriented ensembles of molecules by XUV REMPI and polarization shaping

Cite as: J. Chem. Phys. 151, 074106 (2019); doi: 10.1063/1.5111362

Submitted: 25 May 2019 • Accepted: 16 July 2019 •

Published Online: 15 August 2019



View Online



Export Citation



CrossMark

R. Esteban Goetz,<sup>1</sup>  Christiane P. Koch,<sup>2</sup>  and Loren Greenman<sup>1,a)</sup>

## AFFILIATIONS

<sup>1</sup>Department of Physics, Kansas State University, 116 Cardwell Hall, 1228 N. 17th St., Manhattan, Kansas 66506-2601, USA

<sup>2</sup>Theoretische Physik, Universität Kassel, Heinrich-Plett-Str. 40, D-34132 Kassel, Germany

**Note:** This paper is part of the JCP special collection on Ultrafast Spectroscopy and Diffraction from XUV to X-ray.

<sup>a)</sup>lgreenman@phys.ksu.edu

## ABSTRACT

We report two schemes to generate perfect anisotropy in the photoelectron angular distribution of a randomly oriented ensemble of polyatomic molecules. In order to exert full control over the anisotropy of photoelectron emission, we exploit interferences between single-photon pathways and a manifold of resonantly enhanced two-photon pathways. These are shown to outperform nonsequential ( $\omega$ ,  $2\omega$ ) bichromatic phase control for the example of CHFClBr molecules. We are able to optimize pulses that yield anisotropic photoelectron emission thanks to a very efficient calculation of photoelectron momentum distributions. This is accomplished by combining elements of quantum chemistry, variational scattering theory, and time-dependent perturbation theory.

Published under license by AIP Publishing. <https://doi.org/10.1063/1.5111362>

## I. INTRODUCTION

Modern XUV and x-ray sources are increasing in brightness, time resolution, and phase stability,<sup>1,2</sup> and these advances will lead to the use of light to probe and control the dynamics of electrons in molecules on their natural time scales. Additionally, coincidence measurement techniques<sup>3–5</sup> and laser alignment<sup>6–8</sup> are improving the ability to recover the molecular frame in XUV and x-ray experiments. However, at light sources where it is impractical to perform coincidence experiments, or in systems of growing complexity where alignment or analysis of the fragmentation is difficult, complementary methods are required to obtain sensitive, differential information. The anisotropic photoelectron distributions induced by breaking parity symmetry are one example of a possible complementary technique.<sup>9–24</sup> In the photoelectron circular dichroism (PECD) technique,<sup>9,13,25–33</sup> chiral molecules are used to break parity symmetry and the differential photoelectron angular distribution (PAD) for ionization by left and right circularly polarized light is measured. This technique has recently been extended to time-resolved studies,<sup>34,35</sup> illustrating its promise as

a probe of dynamics. However, in the XUV and x-ray regimes, the techniques for generation and control of highly coherent circularly polarized light sources are limited. In addition, differential techniques complementary to coincidence measurements that can probe the structure and dynamics in achiral molecules are also desired.

An alternative to PECD is the control of anisotropy in a single PAD using multiphoton pathways, where the light fields are used to break parity symmetry.<sup>36</sup> Such studies generally focus on using two-color pulses to manipulate the phase between two quantum pathways. Two-pathway coherent control of the PAD in nonsequential bichromatic ( $\omega$ ,  $2\omega$ ) photoionization has been reported in atomic systems,<sup>16,17,19,37–39</sup> which are invariant under rotation operations. In particular, a high degree of left-right asymmetry ( $\approx 100\%$ ) has been reported in theoretical studies of atomic hydrogen<sup>40</sup> and neon<sup>19</sup> by interfering a single-photon ionization channel and one resonantly enhanced two-photon ionization pathway.

In molecular systems, on the other hand, single and multiphoton ionization processes are highly spherically asymmetric.<sup>41–44</sup>

Consequently, frame-rotation effects can be observed in bichromatic coherent control of asymmetries in the molecular PAD.<sup>15,22,45</sup> In this context, a high degree of anisotropy (100%) has been measured in the phase-controlled bichromatic ionization of aligned molecular NO<sup>15</sup> and it has been calculated with nuclear motion for aligned H<sub>2</sub><sup>+</sup>.<sup>14,20</sup> The sensitivity of the PAD to the field helicity may also be exploited for the purpose of controlling the asymmetry in the PAD. For instance, a high-degree of asymmetry from (prealigned) single-electron H<sub>2</sub><sup>+</sup> was reported in phase-controlled bichromatic ionization using co- and counter-rotating field polarization components of attosecond UV fields.<sup>22</sup>

While the coherent control calculations in Refs. 14, 20, and 22 assume molecular alignment, the experimental conditions might be such that the initial orientation of the target cannot be unambiguously defined. Consequently, an equiprobable orientation distribution is often assumed by integrating over all possible molecular orientations with a homogeneous probability distribution.<sup>46–48</sup> Without laser alignment techniques, the efficiency of two-color control of anisotropy may be obscured by orientation averaging or it may be completely suppressed. Although the orientation averaging approach has become the gold standard for theoretical studies on chiro-optical discrimination in rotationally isotropic media,<sup>23,24,49–51</sup> the question of whether the anisotropy in the PAD persists after the orientation averaging in linearly polarized bichromatic ionization remains yet to be answered.

Polarization-shaped pulses, wherein the instantaneous polarization<sup>52</sup> or helicity changes dynamically over time,<sup>53–58</sup> offer another degree of freedom for control.<sup>55,59,60</sup> However, the efficiency of shaping the polarization of the driving field in the specific context of resonantly enhanced multiphoton ionization (REMPI) to achieve perfect anisotropy in a randomly ensemble of molecules is, to the best of our knowledge, not known. In particular, whether nonsequential bichromatic ( $\omega$ ,  $2\omega$ ) phase control<sup>36</sup> or sequential wave packet evolution-based pump-probe<sup>61</sup> schemes suffice to achieve perfect anisotropy in randomly oriented molecules or whether a more general control scheme based on coherent control<sup>52</sup> is needed remains an open question.

In order to answer these questions, we first show that the anisotropy in linearly polarized bichromatic ionization does persist after orientation averaging. As a second step, we identify the limitations of this approach to achieve perfect anisotropy in a randomly oriented ensemble of CHFClBr molecules. We then demonstrate how to achieve perfect anisotropy by exploiting quantum pathway interferences between single-photon ionization pathways and a manifold of REMPI paths driven by linearly polarized multicolor fields.

Additionally, we investigate the influence of the polarization state (linear, circular left, and right) of the driving field and extend our analysis to the case of polarization shaped pulses. We optimize the time-dependence of the polarization state by combining fields with simultaneous counter-rotating components,<sup>59,60</sup> i.e., by combining multicolor fields circularly polarized along left and right polarization directions. We show that quantum interferences driven by polarization-shaped fields results in perfect anisotropy in the orientation-averaged PAD. We find that the individual contribution of each circularly polarized component induces very modest asymmetry, whereas a combination of components leads to a much larger effect.

We are able to find the optimal REMPI pathways using quantum optimal control theory.<sup>62</sup> This requires a method for calculating the photoionization dynamics of molecules that can be repeated for a number of different laser pulses efficiently. We use a combination of quantum chemistry to describe the bound states, variational scattering theory to calculate dipole matrix elements between bound states and photoionized states, and time-dependent perturbation theory to describe the dynamics. We have implemented this technique in Ref. 24 and have extended it here to pulses with arbitrary polarization state.

This work is organized as follows: In Sec. II, we present the details of the derivation of the orientation-averaged PAD. In Sec. III A, we construct a control scheme based on multiple REMPI pathways and compare its performance in maximizing the anisotropy of the PADs of a randomly oriented ensemble of CHFClBr molecules against that of the two-color coherent control driven by bichromatic ( $\omega$ ,  $2\omega$ ) pulses. Finally, we extend our findings to the case of polarization-shaped pulses in Sec. III B and Sec. IV concludes.

## II. THEORETICAL FRAMEWORK

### A. Laboratory-frame orientation averaged PAD

We first detail our methodology to calculate the orientation averaged photoelectron momentum distribution in the laboratory frame of reference, which is formulated in the strict electric dipole approximation. In what follows, primed and unprimed bold symbols are used to define vector quantities in the fixed laboratory ( $\mathcal{R}'$ ) and molecular ( $\mathcal{R}$ ) frames of reference, respectively, with  $\mathcal{R}$  being rotated relative to  $\mathcal{R}'$  by Euler angles  $\gamma_{\mathcal{R}} = (\alpha, \beta, \gamma)$ .<sup>63</sup> Neglecting relativistic effects and assuming fixed nuclei during the interaction, the Schrödinger equation for the many electron system in  $\mathcal{R}$  reads

$$i \frac{\partial}{\partial t} |\Psi^N(t; \gamma_{\mathcal{R}})\rangle = [\hat{H}_0 - \mathbf{E}(t; \gamma_{\mathcal{R}}) \cdot \hat{\mathbf{r}}] |\Psi^N(t; \gamma_{\mathcal{R}})\rangle, \quad (1)$$

where  $\hat{H}_0 = \hat{H}_0 + \hat{H}_1$  refers to field-free Hamiltonian, with  $\hat{H}_0$  and  $\hat{H}_1$  being the mean-field Fock operator and the residual Coulomb interaction,<sup>64</sup> respectively. Finally,  $\mathbf{E}(t; \gamma_{\mathcal{R}})$  is the electric field in  $\mathcal{R}$ . The polarization components of the driven field are known in the laboratory frame. It can thus be defined in terms of the (fixed) spherical unit vectors,  $\mathbf{e}'_{\mu_0}$ , with  $\mu_0 = \pm 1, 0$ ,<sup>63</sup> relative to  $\mathcal{R}'$ , namely,

$$\mathbf{E}'(t) = \sum_{\mu_0=0,\pm 1} \mathcal{E}'_{\mu_0}(t) \mathbf{e}'_{\mu_0}, \quad (2a)$$

where  $(*)$  denotes the complex conjugation and  $\mathcal{E}'_{\mu_0}(t)$  are the polarization unit components of the field in  $\mathcal{R}'$ . The Cartesian components of the spherical unit vectors are defined in the usual manner and given in Eq. (A1c) in Appendix A. Upon projection of  $\mathbf{e}'_{\mu_0}$  into  $\mathcal{R}$ , as detailed in Appendix A, the molecular-frame orientation-dependent dipole interaction reads

$$\mathbf{E}(t; \gamma_{\mathcal{R}}) \cdot \hat{\mathbf{r}} = \sum_{\mu_0} (-1)^{\mu_0} \mathcal{E}'_{\mu_0}(t) \sum_{\mu} \mathcal{D}_{\mu, -\mu_0}^{(1)}(\gamma_{\mathcal{R}}) \hat{\mathbf{r}}_{\mu}, \quad (2b)$$

where  $\mathcal{D}_{\mu, \mu_0}^{(1)}(\gamma_{\mathcal{R}})$  are the elements of the Wigner rotation matrix.<sup>63,65</sup>

Accounting for one-particle one-hole excitations only, the many-body wave function is described by the TDCIS ansatz<sup>66</sup>

$$|\Psi^N(t; \gamma_{\mathcal{R}})\rangle = \alpha_0(t; \gamma_{\mathcal{R}}) e^{-i\epsilon_0 t} |\Phi_0\rangle + \sum_{i,a} \alpha_i^a(t; \gamma_{\mathcal{R}}) e^{-i\epsilon_i^a t} |\Phi_i^a\rangle + \sum_i \int d\mathbf{k} \alpha_i^k(t; \gamma_{\mathcal{R}}) e^{-i\epsilon_i^k t} |\Phi_i^k\rangle, \quad (3)$$

where  $\alpha_0(t; \gamma_{\mathcal{R}})$ ,  $\alpha_i^a(t; \gamma_{\mathcal{R}})$ , and  $\alpha_i^k(t; \gamma_{\mathcal{R}})$  are time-dependent coefficients and  $|\Phi_0\rangle$  refers to the Hartree-Fock ground state.  $|\Phi_i^a\rangle = \hat{c}_i^\dagger \hat{c}_i |\Phi_0\rangle$  describes the one-particle one-hole excitation from

an initially occupied orbital  $\varphi_i$  to an initially unoccupied Hartree-Fock orbital  $\varphi_a$  with orbital energy  $\epsilon_a$ , whereas  $|\Phi_i^k\rangle$  describes the excitation to scattering continuum state  $\varphi_{\mathbf{k}}$  with energy  $|\mathbf{k}|^2/2$ . We denote the Fock energy of a single determinant as  $\epsilon$ , e.g.,  $\epsilon_0 = \sum_i \epsilon_i$ . For the calculations presented here, we further restrict the configuration space in Eq. (3) to excitations from the highest occupied molecular orbital (HOMO, labeled  $i_0$ ) only. The Hartree-Fock orbitals were obtained using the MOLPRO<sup>67,68</sup> program package at the aug-cc-pVDZ basis set<sup>69</sup> level.

Neglecting the residual Coulomb interaction, the coupled equations for the expansion coefficients read

$$\dot{\alpha}_0(t; \gamma_{\mathcal{R}}) = i \sum_{\mu_0, \mu} (-1)^{\mu_0} \mathcal{D}_{\mu, -\mu_0}^{(1)}(\gamma_{\mathcal{R}}) \mathcal{G}_{\mu_0}^{\mathcal{R}}(t) \left[ \sum_i (\mathbf{r}_{i,i} \cdot \mathbf{e}_\mu) \alpha_0(t; \gamma_{\mathcal{R}}) + \sum_{i,a} (\mathbf{r}_{i,a} \cdot \mathbf{e}_\mu) e^{i(\epsilon_i - \epsilon_a)t} \alpha_i^a(t; \gamma_{\mathcal{R}}) + \sum_i \int d\mathbf{k} (\mathbf{r}_{i,k} \cdot \mathbf{e}_\mu) e^{i(\epsilon_i - \epsilon_k)t} \alpha_i^k(t; \gamma_{\mathcal{R}}) \right], \quad (4a)$$

$$\dot{\alpha}_i^a(t; \gamma_{\mathcal{R}}) = i \sum_{\mu_0, \mu} (-1)^{\mu_0} \mathcal{D}_{\mu, -\mu_0}^{(1)}(\gamma_{\mathcal{R}}) \mathcal{G}_{\mu_0}^{\mathcal{R}}(t) \left[ (\mathbf{r}_{a,i} \cdot \mathbf{e}_\mu) e^{i(\epsilon_a - \epsilon_i)t} \alpha_0(t; \gamma_{\mathcal{R}}) + \sum_{b \neq a} (\mathbf{r}_{a,b} \cdot \mathbf{e}_\mu) e^{i(\epsilon_a - \epsilon_b)t} \alpha_b^b(t; \gamma_{\mathcal{R}}) - \sum_{j \neq i} (\mathbf{r}_{i,j} \cdot \mathbf{e}_\mu) e^{i(\epsilon_j - \epsilon_i)t} \alpha_j^a(t; \gamma_{\mathcal{R}}) + \left( \sum_j \mathbf{r}_{j,j} - \mathbf{r}_{i,i} + \mathbf{r}_{a,a} \right) \cdot \mathbf{e}_\mu \alpha_i^a(t; \gamma_{\mathcal{R}}) + \int d\mathbf{k} (\mathbf{r}_{a,k} \cdot \mathbf{e}_\mu) e^{i(\epsilon_a - \epsilon_k)t} \alpha_i^k(t; \gamma_{\mathcal{R}}) \right], \quad (4b)$$

$$\dot{\alpha}_i^k(t; \gamma_{\mathcal{R}}) = i \sum_{\mu_0, \mu} (-1)^{\mu_0} \mathcal{D}_{\mu, -\mu_0}^{(1)}(\gamma_{\mathcal{R}}) \mathcal{G}_{\mu_0}^{\mathcal{R}}(t) \left[ (\mathbf{r}_{k,i} \cdot \mathbf{e}_\mu) e^{i(\epsilon_k - \epsilon_i)t} \alpha_0(t; \gamma_{\mathcal{R}}) + \sum_b (\mathbf{r}_{k,b} \cdot \mathbf{e}_\mu) e^{-i(\epsilon_b - \epsilon_k)t} \alpha_b^b(t; \gamma_{\mathcal{R}}) - \sum_j (\mathbf{r}_{i,j} \cdot \mathbf{e}_\mu) e^{i(\epsilon_j - \epsilon_i)t} \alpha_j^k(t; \gamma_{\mathcal{R}}) + \left( \sum_j \mathbf{r}_{j,j} - \mathbf{r}_{i,i} + \mathbf{r}_{k,k} \right) \cdot \mathbf{e}_\mu \alpha_i^k(t; \gamma_{\mathcal{R}}) + \int_{\mathbf{k}' \neq \mathbf{k}} d\mathbf{k}' (\mathbf{r}_{k,k'} \cdot \mathbf{e}_\mu) e^{i(\epsilon_k - \epsilon_{k'})t} \alpha_i^{k'}(t; \gamma_{\mathcal{R}}) \right], \quad (4c)$$

where  $\mathbf{r}_{p,q} \cdot \mathbf{e}_\mu = \langle \varphi_p | \hat{r}_\mu | \varphi_q \rangle$ . The coefficients  $\alpha_i^k(t; \gamma_{\mathcal{R}})$  describe the transition amplitude from an initially occupied orbital  $i$  to a continuum state with energy  $\epsilon_k = \epsilon_0 - \epsilon_i + |\mathbf{k}|^2/2$  in the direction  $\mathbf{k}/|\mathbf{k}|$  with respect to the molecular frame of reference,  $\mathcal{R}$ . Since this state is not an eigenstate of the Fock operator,<sup>70</sup> it is an assumption that it can be written as such in Eq. (4c). Similarly,  $\alpha_i^{k'}(t; \gamma_{\mathcal{R}})$  describe this transition in the laboratory frame,  $\mathcal{R}'$ .

To model an ensemble of randomly oriented molecules, we average over all Euler angles  $\gamma_{\mathcal{R}}$ . The orientation-averaged photoelectron momentum distribution is obtained upon integration over  $\gamma_{\mathcal{R}}$  and incoherent summation over the initially occupied contributing orbitals  $i$  in the Hartree-Fock ground state,

$$\frac{d^2 \sigma}{d\epsilon_k d\Omega_{\mathbf{k}'}} = \sum_{i \in \{\text{occ}\}} \int |\alpha_i^{k'}(t; \gamma_{\mathcal{R}})|^2 d^3 \gamma_{\mathcal{R}}, \quad (5)$$

for  $t \rightarrow \infty$  and with  $\mathbf{k}'$  denoting the momentum measured in the laboratory frame. We illustrate how to transform the TDCIS coefficients into the laboratory frame in Sec. II C.

## B. Electron dynamics: Time-dependent perturbative treatment

The photoionization process is captured by the coefficients  $\alpha_i^{k'}(t; \gamma_{\mathcal{R}})$  and requires an accurate description of the scattering components of the wave function in Eq. (3). For a many-electron system with no symmetry, exact numerical simulation of the electron dynamics represents a formidable computational

challenge with prohibitive computational cost. We circumvent this by solving Eq. (4) perturbatively. A second-order approximation is suitable to manipulate quantum interferences between conventional opposite-parity pathways to control the anisotropy of photoelectron emission.<sup>16-19</sup> It can also describe the necessary dynamics of same-parity (two-photon) pathways.<sup>24</sup> Equation (5) simplifies to

$$\frac{d^2 \sigma}{d\epsilon_k d\Omega_{\mathbf{k}'}} \approx \int |\alpha_{i_0}^{k'(1)}(t; \gamma_{\mathcal{R}}) + \alpha_{i_0}^{k'(2)}(t; \gamma_{\mathcal{R}})|^2 d^3 \gamma_{\mathcal{R}} \quad (6)$$

for  $t \rightarrow \infty$  and with  $\alpha_{i_0}^{k'(1,2)}(t; \gamma_{\mathcal{R}})$ , the first (second) order correction. The differential cross section in Eq. (6) can be written in terms of the associated Legendre polynomials  $P_L^M(\cdot)$ ,

$$\frac{d^2 \sigma}{d\epsilon_k d\Omega_{\mathbf{k}'}} = \sum_{L,M} \beta_{L,M}(\epsilon_k) P_L^M(\cos \theta_{\mathbf{k}'}) e^{iM\phi_{\mathbf{k}'}}. \quad (7)$$

Following Ref. 24, we write the photoelectron momentum distribution defined in Eq. (6) in terms of the individual contributions from one- and two-photon ionization processes and their interference,

$$\frac{d^2 \sigma}{d\epsilon_k d\Omega_{\mathbf{k}'}} = \frac{d^2 \sigma^{1ph}}{d\epsilon_k d\Omega_{\mathbf{k}'}} + \frac{d^2 \sigma^{2ph}}{d\epsilon_k d\Omega_{\mathbf{k}'}} + \frac{d^2 \sigma^{int}}{d\epsilon_k d\Omega_{\mathbf{k}'}}. \quad (8)$$

The contribution from one- and two-photon processes defined by the first two terms in the rhs in Eq. (8) reads (for  $n = 1, 2$ )

$$\begin{aligned} \frac{d^2 \sigma^{nph}}{d\epsilon_k d\Omega_{k'}} &= \int \alpha_{i_0}^{(n)k'}(t; \gamma_{\mathcal{R}}) \alpha_{i_0}^{*(n)k'}(t; \gamma_{\mathcal{R}}) d^3 \gamma_{\mathcal{R}} \\ &= \sum_{L,M} \beta_{L,M}^{nph}(\epsilon_k) P_L^M(\cos \theta_{k'}) e^{iM\phi_{k'}}. \end{aligned} \quad (9)$$

The expansion coefficients  $\beta_{L,M}^{1ph(2ph)}(\epsilon_k)$  correspond to the orientation-averaged anisotropy parameters<sup>71</sup> associated with the first (second) order correction. Defining the complex-valued term,

$$\beta_{L,M}^{int} = \int \alpha_{i_0}^{(1)k'}(\gamma_{\mathcal{R}}) \alpha_{i_0}^{*(2)k'}(\gamma_{\mathcal{R}}) d^3 \gamma_{\mathcal{R}}, \quad (10)$$

the contribution from the interfering pathways to the photoelectron spectrum reads

$$\begin{aligned} \frac{d^2 \sigma^{int}}{d\epsilon_k d\Omega_{k'}} &= \int \left( \alpha_{i_0}^{(1)k'}(t; \gamma_{\mathcal{R}}) \alpha_{i_0}^{*(2)k'}(t; \gamma_{\mathcal{R}}) + c.c. \right) d^3 \gamma_{\mathcal{R}} \\ &= \sum_{L,M} \left( \beta_{L,M}^{int}(\epsilon_k) e^{iM\phi_{k'}} + c.c. \right) P_L^M(\cos \theta_{k'}). \end{aligned} \quad (11)$$

First- ( $\alpha_{i_0}^{k'(1)}$ ) and second-order ( $\alpha_{i_0}^{k'(2)}$ ) terms describe direct single-photon photoionization from  $\varphi_{i_0}$  to  $\varphi_{k'}$  and resonant two-photon photoionization from  $\varphi_{i_0}$  to  $\varphi_{k'}$  via different unoccupied orbitals  $\varphi_a$ , respectively.

### C. Variational scattering states

The scattering states required for the evaluation of the dipole matrix elements are obtained from variational scattering theory.<sup>72-74</sup> Assuming no relaxation of the contributing orbitals, the total many-body wave function  $\Phi_i^k(\mathbf{r}_1, \dots, \mathbf{r}_N)$  can be defined, for any  $i \in \{\text{occ}\}$ , as an antisymmetrized product,

$$\Phi_i^k(\mathbf{r}_1, \dots, \mathbf{r}_N) = \mathcal{A}_N [\varphi_k^-(\mathbf{r}_N); \Phi_i(\mathbf{r}_1, \dots, \mathbf{r}_{N-1})], \quad (12a)$$

where  $\varphi_k^-(\mathbf{r}_N)$  corresponds to the (molecular-frame) scattering component of the wave function and  $\Phi_i(\mathbf{r}_1, \dots, \mathbf{r}_{N-1})$  corresponds to the remaining  $N - 1$  electron final state after ionization. We obtain  $\varphi_k^-(\mathbf{r})$  by solving the scattering problem

$$\left[ -\frac{\nabla^2}{2} - \frac{1}{r} + \hat{\mathbf{V}} - \frac{k^2}{2} \right] \varphi_k^-(\mathbf{r}) = 0, \quad (12b)$$

with scattering boundary conditions<sup>75,76</sup> for the outgoing wave  $\varphi_k^-(\mathbf{r})$  at large distances  $\mathbf{r} \rightarrow \infty$ , and where  $\hat{\mathbf{V}}(\mathbf{r})$  describes the short-range part of the electron-ion interaction. Equation (12b) and its dipole matrix elements are computed using a locally modified version of the ePolyScat program package.<sup>72-74</sup> The bound unoccupied Hartree-Fock orbitals that are kept in the time-dependent perturbation expansion are chosen to be those that are orthogonal to the scattering orbitals. In this manner, Gaussian orbitals that attempt to represent continuum states are discarded. In the molecular frame, the direction of photoelectron emission is obtained by expanding the scattering wave function into spherical harmonics,

$$\varphi_k^-(\mathbf{r}) = \sum_{\ell,m} \varphi_{k,\ell,m}^-(\mathbf{r}) Y_m^\ell(\theta_k, \phi_k), \quad (13a)$$

where  $\theta_k$  and  $\phi_k$  correspond to the polar and azimuthal angles of photoelectron emission in the molecular frame, respectively. In the laboratory frame, this direction is defined by the angles  $(\theta_{k'}, \phi_{k'})$ , which is obtained by projecting Eq. (13a) into the laboratory frame. In this frame, the scattering states take the form,

$$\varphi_{k'}^-(\mathbf{r}) = \sum_{\ell,m,m'} \varphi_{k,\ell,m}^-(\mathbf{r}) \mathcal{D}_{m,m'}^{(\ell)\dagger}(\gamma_{\mathcal{R}}) Y_{m'}^\ell(\theta_{k'}, \phi_{k'}). \quad (13b)$$

Applying first-order time-dependent perturbation theory to Eq. (4a) and evaluating the individual matrix elements of Eq. (13a) result in

$$\begin{aligned} \alpha_{i_0}^{k'(1)}(t; \gamma_{\mathcal{R}}) &= i \sum_{\mu_0, \mu} (-1)^{\mu_0} \sum_{\ell,m,m'} \mathcal{D}_{\mu,-\mu_0}^{(1)}(\gamma_{\mathcal{R}}) \mathcal{D}_{m',m}^{(\ell)\dagger}(\gamma_{\mathcal{R}}) (\mathbf{r}_{k,\ell,m;i_0} \cdot \mathbf{e}_\mu) \\ &\quad \times Y_{m'}^\ell(\theta_{k'}, \phi_{k'}) \int_{-\infty}^t e^{i(\epsilon_k - \epsilon_{i_0})t'} \mathcal{E}_{\mu_0}^\sigma(t') dt'. \end{aligned} \quad (14)$$

The dipole matrix element  $\mathbf{r}_{k,\ell,m;i_0} = \langle \varphi_{k,\ell,m}^- | \hat{\mathbf{r}} | \varphi_{i_0} \rangle$  now displays indices for the partial wave quantum numbers  $\ell$  and  $m$  of the continuum orbital and the ionized orbital  $\varphi_{i_0}$ , respectively. Similarly, the expression for the second order correction of the scattering component along the direction of photoelectron emission  $(\theta_{k'}, \phi_{k'})$  relative to the laboratory frame becomes

$$\begin{aligned} \alpha_{i_0}^{k'(2)}(t; \gamma_{\mathcal{R}}) &= - \sum_{\mu_0, \nu_0} (-1)^{\mu_0 + \nu_0} \sum_{\mu, \nu} \mathcal{D}_{\mu,-\mu_0}^{(1)}(\gamma_{\mathcal{R}}) \mathcal{D}_{\nu,-\nu_0}^{(1)}(\gamma_{\mathcal{R}}) \sum_{\ell,m,m'} \mathcal{D}_{m',m}^{(\ell)\dagger}(\gamma_{\mathcal{R}}) Y_{m'}^\ell(\theta_{k'}, \phi_{k'}) \left[ (\mathbf{r}_{k,\ell,m;i_0} \cdot \mathbf{e}_\mu) \sum_i (\mathbf{r}_{i,i} \cdot \mathbf{e}_\nu) \int_{-\infty}^t e^{-i(\epsilon_{i_0} - \epsilon_k)t'} \mathcal{E}_{\mu_0}^\sigma(t') \right. \\ &\quad \left. \times \int_{-\infty}^{t'} \mathcal{E}_{\nu_0}^\sigma(t'') dt'' dt' + \sum_b (\mathbf{r}_{k,\ell,m;b} \cdot \mathbf{e}_\mu) (\mathbf{r}_{b,i_0} \cdot \mathbf{e}_\nu) \int_{-\infty}^t e^{-i(\epsilon_b - \epsilon_k)t'} \mathcal{E}_{\mu_0}^\sigma(t') \int_{-\infty}^{t'} e^{-i(\epsilon_{i_0} - \epsilon_b)t''} \mathcal{E}_{\nu_0}^\sigma(t'') dt'' dt' \right]. \end{aligned} \quad (15)$$

In Eq. (15), we further assume that the last two terms corresponding to Eq. (4c) can be neglected, which is justified by the absence of IR and high-energy XUV photon energies—that are required to make the corresponding time integrals nonzero—in all pulses considered here.

### D. Laboratory-frame orientation-averaged anisotropy parameters

The laboratory-frame orientation-averaged anisotropy parameters associated with one- and two-photon ionization pathways and their interference defined in Eqs. (9) and (10) can be obtained using

the expressions defined in Eqs. (14) and (15). Derivation of the laboratory-frame anisotropy parameters involves cumbersome but straightforward angular momentum algebra. We give explicit details of the derivations in Appendix B. Here, we provide only their ellipticity dependence in the view of listing a few selection rules and requirements for nonvanishing asymmetry in the resulting angular distribution when averaging over all orientations.

The anisotropy parameters  $\beta_{L,M}^{1ph}(\epsilon_k)$ , associated with the one-photon ionization pathway (cf. Appendix B), can be expressed as

$$\beta_{L,M}^{1ph}(\epsilon_k) = \sum_{\mu_0, \mu'_0} c_{\mu_0, \mu'_0}^{(1ph)}(L) \begin{pmatrix} 1 & 1 & L \\ -\mu_0 & \mu'_0 & -M \end{pmatrix}. \quad (16a)$$

The exact form for the coefficients  $c_{\mu_0, \mu'_0}^{(1ph)}(L)$  is given in Appendix B1. In particular for linearly polarized fields, i.e.,  $\mu_0 = \mu'_0 = 0$ , the Wigner  $3j$ -symbol in Eq. (16a) vanishes for  $L$  odd. Consequently, first order processes do not contribute to the asymmetry. For circularly polarized light, however,  $\mu_0$  and  $\mu'_0$  can take values  $\pm 1$ , which would lead to nonvanishing contribution for  $L = 1$  and  $M = 0$  provided that cancellations upon summation over the bound-continuum dipole matrix elements with opposite sign “ $m$ ” magnetic quantum number, here absorbed in the coefficients  $c_{\mu_0, \mu'_0}^{(1ph)}$ , do not occur, i.e., for chiral molecules.<sup>46</sup> The anisotropy parameters associated with second-order processes read

$$\beta_{L,M}^{2ph}(\epsilon_k) = \sum_{\substack{\mu_0, \nu_0 \\ \mu'_0, \nu'_0 \\ Q_1, Q_2}} c_{\mu_0, \nu_0, \mu'_0, \nu'_0, Q_1, Q_2}^{(2ph)}(L) \begin{pmatrix} 1 & 1 & Q_1 \\ -\mu_0 & -\nu_0 & \mu_0 + \nu_0 \end{pmatrix} \\ \times \begin{pmatrix} 1 & 1 & Q_2 \\ -\mu'_0 & -\nu'_0 & \mu'_0 + \nu'_0 \end{pmatrix} \begin{pmatrix} Q_1 & Q_2 & L \\ -\mu_0 - \nu_0 & \mu'_0 + \nu'_0 & -M \end{pmatrix}. \quad (16b)$$

Derivation and explicit form for the coefficients  $\beta_{L,M}^{2ph}(\epsilon_k)$  are detailed in Appendix B2. The selection rules for two-photon process are analogous to that described for the one-photon counterpart. In particular, the third Wigner symbol in Eq. (16b) vanishes for  $L$  odd for linearly polarized fields as the first and second Wigner symbols vanish for odd  $Q_1$  and  $Q_2$ , respectively.

Finally, in Appendix B3, we show that the laboratory-frame orientation-averaged anisotropy parameter associated with the interference between both photoionization pathways, defined in Eq. (10), has the following structure:

$$\beta_{L,M}^{int}(\epsilon_k) = \sum_{Q_1, Q_2} \sum_{\mu_0, \mu'_0} \sum_{\nu_0} c_{\mu_0, \mu'_0, \nu_0, Q_1, Q_2}^{(int)}(L) \\ \times \begin{pmatrix} 1 & 1 & Q_2 \\ -\mu'_0 & -\nu_0 & \mu'_0 + \nu_0 \end{pmatrix} \begin{pmatrix} 1 & Q_2 & L \\ -\mu_0 & \mu'_0 + \nu_0 & -M \end{pmatrix}. \quad (16c)$$

In contrast to Eqs. (16a) and (16b), the interference between one- and two-photon ionization pathways may lead to nonvanishing anisotropy parameters for  $L$  odd when the driving field is linearly polarized. This feature persists even after the orientation averaging. In fact, the second Wigner symbol in Eq. (16c) does not vanish for  $L$  odd and  $Q_2$  even, for  $M = 0$ , when  $\mu_0 = \mu'_0 = \nu_0 = 0$ . Even values for  $Q_2$  are allowed by the first Wigner  $3j$ -symbol. In the following,

we describe our optimization approach to manipulate the anisotropy parameters using different photoionization schemes and polarization configurations in the quest to maximize the anisotropy in the photoelectron emission.

### E. Control of the photoionization dynamics

In order to control the photoionization dynamics, we consider coherent control of wave packet interference mediated by linearly polarized or polarization shaped pulses. In the first instance, the pulse is assumed to be linearly polarized—parallel to the  $\mathbf{e}'_z = \mathbf{e}'_0$  axis—and defined as a coherent superposition of  $N$  subpulses,

$$\mathbf{E}(t) \cdot \mathbf{e}'_0 = \mathcal{E}'_0(t) = \sum_{j=1}^N \mathcal{E}'_{0,j}(t), \quad (17a)$$

where  $\mathcal{E}'_{0,j}(t)$  is the subpulse carrying the frequency  $\omega_j$  and parameterized according to

$$\mathcal{E}'_{j,0}(t) = h_j(t - \tau_j) \cos \Omega_j(t), \quad (17b)$$

with  $\Omega_j(t) = \omega_j(t - \tau_j) + \phi_j$  and where  $h_j(\cdot)$  is a Gaussian envelope of the form

$$h_j(t - \tau_j) = E_{0,j} \times e^{-(t-\tau_j)^2/2\sigma_j}. \quad (17c)$$

The pulse parameters  $E_{0,j}$ ,  $\omega_j$ , and  $\phi_j$  define the peak field amplitude, central frequency, and carrier envelope phase of the  $j$ th subpulse with full width at half maximum FWHM =  $2\sqrt{2 \ln 2} \sigma_j$  whose peak intensity is delayed by  $\tau_j$  with respect to  $t = 0$ .

For polarization-shaped fields, we consider pulses with circular right (CRP) and left (CLP) rotating polarization directions and define the driving field as a linear combination thereof,

$$\mathbf{E}'(t) = \mathbf{E}'_R(t) + \mathbf{E}'_L(t). \quad (18)$$

The CRP and CLP components are defined from the point of view of the emitter and parameterized following the guidelines detailed in Appendix C.

For further inspection of the electron dynamics driven by polarization shaped pulses, we define  $\zeta_j(t)$  as the helicity of the subpulse carrying the frequency  $\omega_j$ , which we write in terms of the differential quantity<sup>59,77</sup>

$$\zeta_j(t) = \frac{|\mathbf{E}'_{R,j}(t)| - |\mathbf{E}'_{L,j}(t)|}{|\mathbf{E}'_{R,j}(t)| + |\mathbf{E}'_{L,j}(t)|}, \quad (19)$$

with  $\mathbf{E}'_{R,j}(t)$  ( $\mathbf{E}'_{L,j}(t)$ ) being the portion of the field with CRP (CLP) carrying the frequency component  $\omega_j$ .

The photoelectron observable  $\mathcal{I}(\epsilon, \theta_{k'})$  is an energy- and angle-resolved measurable quantity proportional to a photoelectron probability distribution defined in Eq. (8) and given by<sup>24</sup>

$$\mathcal{I}(\epsilon, \theta_{k'}) \propto \left. \frac{d^2 \sigma}{d\epsilon_k d\Omega_{k'}} \right|_{\phi_{k'} = \pi/2}. \quad (20)$$

We define the intensity-normalized anisotropy of the PAD as

$$\mathcal{A}(\epsilon_k, \theta_{k'}) = \frac{\mathcal{I}(\epsilon_k, \theta_{k'}) - \mathcal{I}(\epsilon_k, \pi - \theta_{k'})}{\mathcal{I}_0}, \quad (21)$$

where  $\theta_{k'}$  is defined by the photoelectron direction of emission with respect to the light propagation direction for circularly polarized light or with respect to the light polarization direction for linearly polarized fields and where  $\mathcal{I}_0$  corresponds to the photoelectron peak intensity

$$\mathcal{I}_0 = \max_{\epsilon_k, \theta_{k'}} \mathcal{I}(\epsilon_k, \theta_{k'}). \quad (22)$$

Next, we define the optimization problem by

$$\arg \max_{\mathbf{E}'(t) \in U} \left\{ \max_{\epsilon_k, \theta_{k'}} |\mathcal{A}(\epsilon_k, \theta_{k'})| \right\}, \quad (23)$$

where  $U$  is the subset of feasible solutions, i.e., constraints that the parameters defining each component of the electric field  $\mathbf{E}'(t)$  must fulfill such as maximal peak intensity, maximal duration (FWHM), allowed frequency components, or maximal time-delay between two distinct frequency components. The functional form of the driving field is parameterized according to Eq. (17) for linearly polarized fields and using Eqs. (C1c) and (C1d) for fields with time dependent helicity. These parameters are optimized using a gradient-free sequential update-based method detailed in Ref. 78 to maximize the anisotropy of photoelectron emission probability as defined in Eq. (23).

Throughout the text, the term anisotropy will be used to refer to the quantity defined in Eq. (21), which will be expressed in percentage (of  $\mathcal{I}_0$ ). Perfect anisotropy is thus only obtained when, for some optimal kinetic energy  $\epsilon_k^*$  and emission angle  $\theta_{k'}^*$ , the anisotropic component of the photoelectron signal corresponds to the peak intensity  $\mathcal{I}_0$ .

### III. NUMERICAL RESULTS

#### A. Photoelectron anisotropy with linearly polarized fields

We start by considering nonsequential phase-controlled bichromatic ( $\omega, 2\omega$ ) ionization from a randomly oriented ensemble of CHBrClF molecules driven by linearly polarized fields, with polarization direction parallel to the  $z'$ -axis. Figure 1 shows the left-right anisotropy of photoelectron emission as a function of the photon

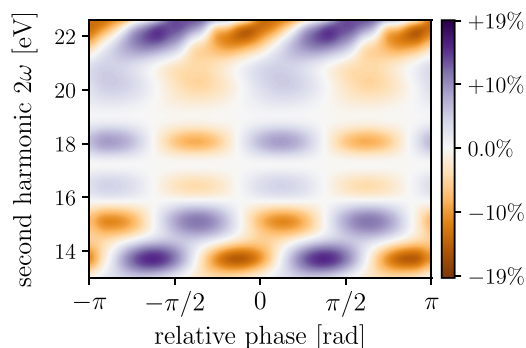


**FIG. 1.** Left-right asymmetry in the PAD as a function of the photon energy and phase difference between the fundamental and second harmonic of a linearly polarized bichromatic ( $\omega, 2\omega$ ) pulse.

energy (second harmonic) and relative phase between both colors. This corresponds to the typical scenario discussed in Refs. 16, 17, 19, and 37–40. The asymmetries shown in Fig. 1 were obtained by considering a 1 : 2 ratio of fundamental to second harmonic, with  $I_0 = 10^{11}$  W/cm<sup>2</sup> for the fundamental. A pulse with a width of 23 fs was used for both colors. This ratio leads to comparable ionization yields from both pathways, inducing a noticeable break of symmetry in the PAD, which is independent of the chiral nature of the target<sup>16,17,36,40</sup> as the field is linearly polarized. The anisotropy originates from a coherent wave packet interference between single- and two-photon photoionization pathways. Periodic oscillations of the anisotropy as a function of the relative phase can be observed, confirming the coherent nature of the control mechanism. Overall, the left-right anisotropy exhibits moderate values not exceeding  $\pm 20\%$  for the chosen field parameters. In what follows, we will discuss the efficiency and limitations of bichromatic coherent control for achieving perfect anisotropy in randomly oriented photoionized molecules.

To answer the question whether perfect anisotropy (100%) in a randomly oriented sample of molecules is achievable by coherent control using suitably shaped ionizing pulses beyond the nonsequential bichromatic case, we optimize multicolor fields, defined in Eq. (17), first constraining the polarization state to linear and the maximal peak intensity to not exceed  $1.0 \times 10^{12}$  W/cm<sup>2</sup>. This intensity threshold has been found to be an appropriate upper limit for the validity of the perturbation treatment in bichromatic photoionization studies.<sup>16</sup> Figure 2(a) displays the left-right asymmetry in the PAD obtained upon optimization of the linearly polarized multicolor field. The corresponding PAD, shown in Fig. 2(b), exhibits perfect left-right anisotropy (100%) exactly at a photoelectron kinetic energy of 10 eV with maximal probability of photoelectron emission parallel to the field polarization axis and minimal probability of emission antiparallel to this axis. In order to investigate the coherent mechanism leading to the anisotropy of 100% displayed in Fig. 2(a), we analyze the optimized frequency components and spectral phases in Fig. 3. In detail, the photon energy distributions shown in Fig. 3 at 7.1 eV and 14.8 eV ensure resonant photoionization of the HOMO—through the LUMO—to a final photoelectron kinetic energy of 10 eV. The lowest photon energy of 7.1 eV corresponds to the resonant transition energy between the HOMO and LUMO, with orbital energies corresponding, at the aug-cc-pVDZ level, to  $-11.878$  eV and  $-4.803$  eV, respectively. Interestingly, the double-peaked photon energy distribution shown in Fig. 3 at 10.8 eV and 11.1 eV has a fourfold purpose with nested contributions to the excitation-ionization steps: It contains

- the required photon energy of 10.97 eV (first peak) to excite the transition HOMO  $\rightarrow$  LUMO + 1,
- the photon energy of 11.063 eV (second peak) to resonantly excite the transition HOMO  $\rightarrow$  LUMO + 2,
- the appropriate photon energy of 10.97 eV (second peak) to ionize the LUMO + 1 to a photoelectron kinetic energy of exactly 10 eV, and
- within the spectral distribution around 10.8 eV, the photon energy of 10.814 eV to ionize the LUMO + 2 (first peak) also at 10 eV.

Finally, the spectrum of the optimized field also contains the photon energy of 21.875 eV—at an intensity of  $4.11 \times 10^9$  W/cm<sup>2</sup>—which is required to ionize the HOMO at a photoelectron kinetic energy of

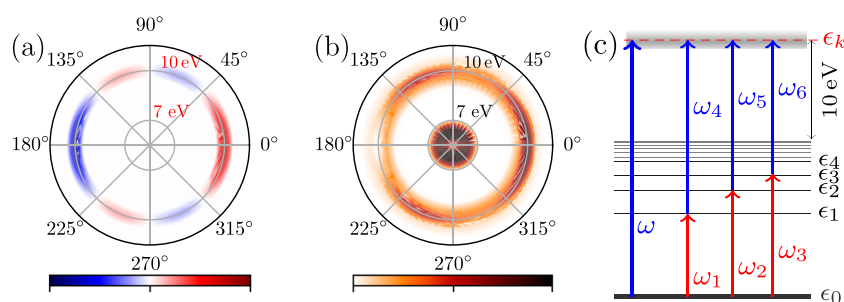


**FIG. 2.** (a) Optimized anisotropy in the PAD corresponding to the multiple-REMPI scheme, achieving 100% of asymmetry at a photoelectron kinetic energy of 10 eV and angles  $\theta_{k'} = 180^\circ$  and  $\theta_{k'} = 0^\circ$ . (b) Corresponding photoelectron momentum distribution with zero probability of photoelectron emission at  $\theta_{k'} = 180^\circ$  and maximal ionization probability at  $\theta_{k'} = 0^\circ$ . (c) Schematic energy representation of the photoionization process leading to the observed asymmetry.

10 eV. Simultaneous removal of the frequency components around (i) 7.1 eV and 10.8–11.1 eV in Fig. 3 or (ii) those around 10.8–11.1 eV and 14.8 eV, or (iii) that centered at 21.9 eV alone results in zero left-right asymmetry. In cases (i) and (ii), the required photon energies to induce resonantly enhanced two-photon ionization at a photoelectron energy of 10 eV probing the first three lowest unoccupied molecular orbitals are inaccessible. In case (iii), these even-parity photoionization pathways are enabled but the odd-parity pathway is disabled. For linearly polarized light, interferences between same-parity photoionization pathways do not break the asymmetry as discussed in Sec. II D. Consequently, no anisotropy is observed in (iii). Conversely, removing only the photon energies of 10.8–11.1 eV, which induce resonant ionization probing the LUMO + 1 and LUMO + 2, or those corresponding to 7.1 eV and 14.8 eV, which promote resonant ionization through the LUMO, results in nonvanishing anisotropy at 10 eV. These observations suggest a control mechanism based on coherent wave packet interferences mediated by one-photon ionization and a manifold of two-photon ionization

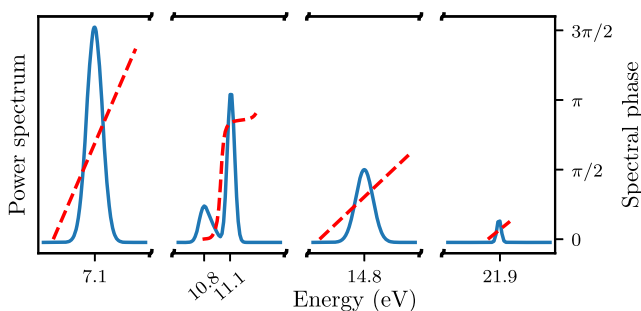


**FIG. 3.** Optimized electric field spectrum (blue line) leading to the left-right anisotropy of photoelectron emission of 100% shown in Fig. 2. The optimal field contains the required photon energies to generate two-photon (7.1–14.8 eV) and single-photon (21.9 eV) pathways that constructively interfere at 10 eV, as schematized in Fig. 2(c): The low frequency component at 7.1 eV in resonantly excites the LUMO. The peaks at 10.8 and 11.1 eV—within their bandwidth—resonantly excite the LUMO +  $j$  orbitals, for  $j > 1$ . The energy required for the ionization of the resonantly excited LUMOs at a photoelectron kinetic energy of 10 eV is available within the spectral bandwidth around the peak at 14.8 eV. The 21.9 eV frequency is responsible for single-photon ionization of the LUMO at a photoelectron kinetic energy of 10 eV.

pathways. Furthermore, altering the spectral phase shown in Fig. 3, while keeping the power spectrum unchanged, dramatically alters the resulting asymmetry, leading to significantly smaller magnitudes (below 10%, depending on the spectral phase modifications), confirming the coherent nature of the control mechanism. We therefore conclude that the enhancement mechanism is mediated by constructive quantum interferences between the different portions of the coherent photoelectron wave packet resulting from the odd-parity single-photon ionization channel and a manifold of even-parity resonant ionization pathways involving the first three molecular excited states.

Asymmetries in the PADs are well-known to be sensitive to the photoelectron kinetic energy see, e.g., Refs. 19 and 40 for bichromatic ionization in linearly polarized fields. In order to disentangle the contributions from the final continuum state (here defined by the continuum state with energy 10 eV at which the multiple-REMPI achieves perfect anisotropy) and those originating from the ionization pathways (defined by the multiple-REMPI paths), we optimize linearly polarized fields to maximize the left-right asymmetry at the same photoelectron kinetic energy of 10 eV, but constraining the optimized pulse spectrum to bichromatic ( $\omega$ ,  $2\omega$ ) components. This corresponds to (fixed) photon energies carried by the fundamental and second harmonic of  $\omega = 10.939$  eV and  $2\omega = 21.878$  eV, respectively. It is worth noting that both control approaches, namely, multiple-REMPI and bichromatic schemes, share the photon energy of  $2\omega = 21.878$  eV and both being optimized at the same photoelectron kinetic energy, any difference in the outcome is thus solely due to an intermediate-pathway effect.

Figure 4(a) shows the maximal achievable anisotropy at a photoelectron energy of 10 eV obtained with the linearly polarized optimized bichromatic ( $\omega$ ,  $2\omega$ ) pulse. With a maximal left-right asymmetry of 52% at 10 eV, the performance of the bichromatic ( $\omega$ ,  $2\omega$ ) ionization scheme is significantly inferior to the multiple-REMPI scheme. The smaller asymmetry obtained in the bichromatic scenario can be explained by the fact that resonant excitation driven by the fundamental is not fully achieved. In fact, the two-photon pathway is in resonance at  $-0.939$  eV, which lies between the orbital energies of LUMO + 1 ( $-0.974$  eV) and LUMO + 2 ( $-0.8136$  eV), as depicted in Fig. 4(b).

Therefore, for an objective comparison between the bichromatic and multiple-REMPI approaches, we further optimize linearly polarized fields using both schemes but within a range of

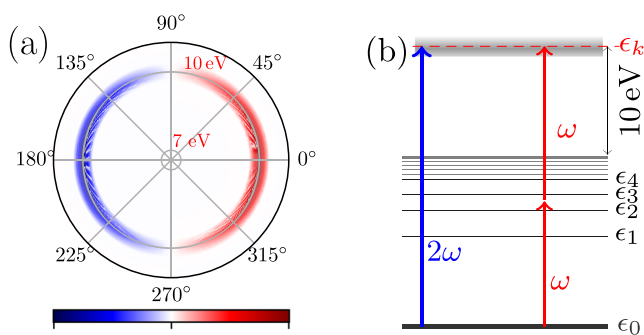


**FIG. 4.** (a) For a photoelectron kinetic energy of 10 eV, a maximal anisotropy of 52% is obtained with the optimized bichromatic ( $\omega, 2\omega$ ), in contrast to 100% for the multiple-REMPI scheme shown in Fig. 2. (b) Photoionization scheme for the optimized bichromatic ( $\omega, 2\omega$ ) pulse.

different photoelectron kinetic energies. Figure 5 displays the maximal achievable left-right asymmetry obtained with both, the multiple-REMPI (solid-blue line) and the bichromatic ( $\omega, 2\omega$ ) (dotted-dashed red line) schemes. The oscillations in Fig. 5 illustrate the sensitivity of the anisotropy to the final continuum state for the different control schemes. Nevertheless, and with no exception, the multiple-REMPI scheme systematically outperforms the bichromatic ( $\omega, 2\omega$ ) counterpart.

It is worth noting that decreasing the number of (resonant) interfering paths results in an overall decrease in the left-right asymmetry. For instance, the 3-color (LUMO) case shown in Fig. 5 (dashed-green line) corresponds to a particular case of the multiple-REMPI scheme where only a single even-parity two-photon pathway, in resonance with the LUMO, interferes with the odd-parity ionization channel.

## B. Optimal control in multicolor polarization-shaped fields

Extension of the multiple-REMPI scheme to circularly polarized fields provides an additional degree of freedom for the

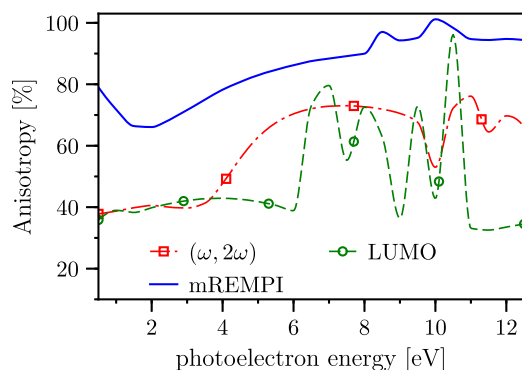


**FIG. 5.** Maximal achievable anisotropy for different photoionization schemes: linearly polarized bichromatic ( $\omega, 2\omega$ ) pulse (dotted-dashed red line), multiple-REMPI (filled blue line), and 3-color (LUMO) case (dashed-green) discussed in the text.

possible interfering pathways. Here, quantum interferences between opposite-parity and even-parity two-photon ionization paths can be exploited to exert control over the forward-backward asymmetry in the photoelectron emission probability.<sup>24</sup> We find that fixing the field polarization state to either left- or right-circular for all optical pathways leads to a maximal forward-backward asymmetry of 68% at 6.5 eV and 64% at 10 eV. These results clearly indicate that the orientation-averaged asymmetry in PAD is sensitive to the details of the polarization of the driven field.

It is nevertheless possible to retrieve perfect forward/backward anisotropy, i.e., 100%, in the direction of photoelectron emission by shaping the polarization state of the driving field in time. In other words, we render the helicity of the field polarization time-dependent. This can be achieved by introducing different pulse durations, phases, and time delays by projection in counter-rotating directions.<sup>59</sup>

We test this approach to maximize the forward-backward photoelectron emission probability at a photoelectron kinetic energy of 10 eV. This energy corresponds to the photoelectron kinetic energy at which a perfect anisotropy of 100% was obtained using the optimized linearly polarized pulse (cf. Fig. 2). Figure 6(a) displays the resulting asymmetric component of the PAD. The optimized forward-backward anisotropy amounts to 100% at the kinetic photoelectron energy  $\epsilon_k^*$  of 10 eV along the direction  $\theta_{k'}^* = 135^\circ$ . The optimized momentum distribution shown in Fig. 6(b) exhibits vanishing emission probability in the direction defined by  $\theta_{k'} = 45^\circ$  and maximal photoemission probability at  $135^\circ$  for 10 eV. Here,  $\theta_{k'}$  corresponds to the polar angle with respect to the light propagation direction—assumed to define the  $z'$ -axis—and corresponding to  $\theta_{k'} = 0^\circ$ . The optimized field with time-dependent helicity is shown in Figs. 7(a) and 7(b), showing the optimized circularly right and left rotating components, respectively. The multicolor field with time-dependent helicity is able to reach a forward-backward asymmetry of 100%, in contrast to 64% reached by optimizing the field with fixed (left or right) helicity, i.e., time-independent helicity.

In order to quantify the main contribution to the enhancement, we further inspect the spectral components for each

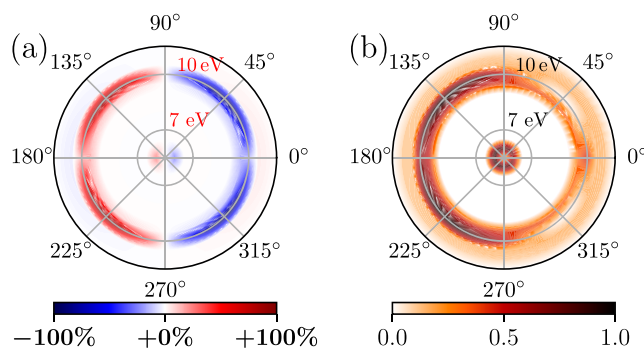


**FIG. 6.** (a) Asymmetric component in the forward-backward photoelectron emission probability obtained with the optimized multicolor field with time-dependent helicity. The field has been optimized to maximize the anisotropy of photoelectron emission at a photoelectron kinetic energy of 10 eV. Corresponding photoelectron momentum distribution shown in (b).

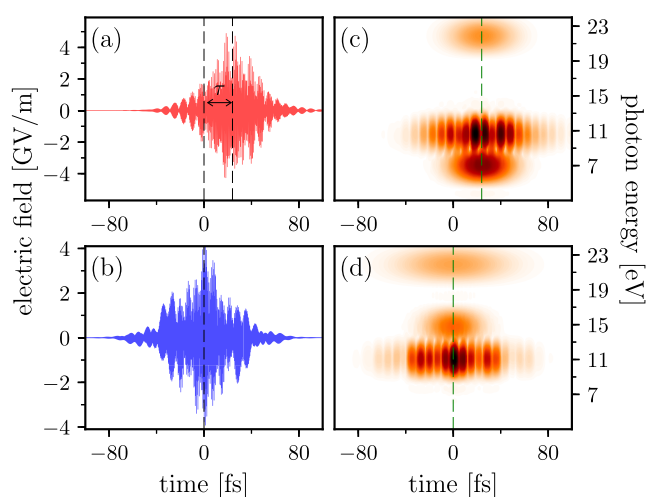


**FIG. 7.** Projection of the circularly right [(a) and (c)] and left [(b) and (d)] rotating components of the optimized field into the  $x'$ -axis. A time delay  $\tau \approx 24$  fs between both counter-rotating components is observed in the temporal [(a) and (b), dashed black lines] as well as in the frequency domain [cf. (c) and (d), dashed green lines]. However, within a given rotating direction, left or right, all frequency components are perfectly synchronized.

counter-rotating component. Figures 7(c) and 7(d) display the projections onto the  $x'$ -axis of the time-frequency distribution for the circularly right (c) and left (d) rotating fields. By comparing Figs. 7(c) and 7(d), it is apparent that a non-negligible time delay separates the time-frequency distribution along both counter-rotating directions, which could also already be noted in Figs. 7(a) and 7(b). Interestingly, for a given rotation direction—left or right—all frequency components are synchronized with no appreciable time-delay among them [cf. Figs. 7(c) and 7(d)].

Another remarkable difference between the optimized right and left rotating fields concerns their spectral distribution. While the optimized rotating fields,  $E_R(t)$  and  $E_L(t)$  share the photon energies of 10.8 eV, 10.9 eV, 11.06 eV, and 21.87 eV [cf. Figs. 7(b) and 7(d)], the photon energy required for the excitation of the LUMO (7.074 eV) is only contained in the circularly right polarized component [cf. Fig. 7(b)]. Conversely, the photon energy of 14.803 eV—required for the ionization of the LUMO—is only present along its counter-rotating counterpart [cf. Fig. 7(d)]. The Wigner-Ville distribution function in Figs. 7(c) and 7(d) indicates that the photon energies required for the excitation and ionization of the LUMO—7.05 eV and 14.80 eV—share a common time window of about  $\approx 60$  fs—which can also be seen in Figs. 8(a) and 8(c)—suggesting nonsequential resonant excitation-ionization probing the LUMO as part of the optimal ionization mechanism: the resonant excitation of the LUMO is mediated by the clockwise rotating component, whereas ionization at a photoelectron kinetic energy of 10 eV is ensured by the counter-clockwise component of the field.

The electron dynamics involving the LUMO + 1 and LUMO + 2 turns out to be more complicated as both counter-rotating fields share the photon energies centered around 10.8 eV and 11.06 eV, which we recall, have the fourfold purpose of exciting and ionizing

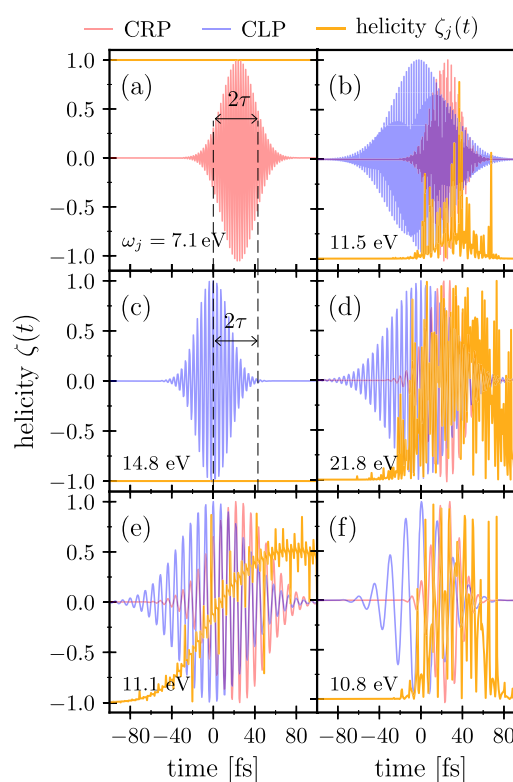


**FIG. 8.** (a)–(f) Electric field helicity  $\zeta_j(t)$  for a subpulse carrying the frequency  $\omega_j$  as a function of time (solid-orange line). The optimized field contains subpulses carrying frequencies  $\omega_j$  with simultaneous projections along both counter-rotating polarization directions. When both counter-rotating components share the same frequency  $\omega_j$ , the time-delay between the subpulses carrying  $\omega_j$  has a twofold role: first, it synchronizes the resonant excitation-ionization processes between the contributing resonant photoionization paths and second, it defines the temporal profile of the helicity (along with pulse FWHM, phases, peak intensity) to achieve 100% anisotropy by exploiting the sensitivity of the PAD to the temporal changes of the field polarization direction, which was not possible when a circularly polarized field with constant helicity, i.e.  $[\zeta(t) = \pm 1]$ , was prescribed to achieve the same goal.

the LUMO + 1 and LUMO + 2 at a final photoelectron energy of 10 eV, as already discussed in the case of linearly polarized fields in Sec. III A. Indeed, according to the time-frequency distribution in Fig. 7(d), the left rotating component induces nonsequential excitation-ionization of the LUMO + 1 and LUMO + 2. In addition, the circularly right polarized component of the field does so, although slightly later. However, since both counter-rotating components share a common time-window, a rich but complex resonant excitation-ionization—probing the LUMO + 1 and LUMO + 2—driven by the portion of the field with time-dependent helicity occurs.

Finally, the part of the field carrying a photon energy of 21.878 eV—which induces single-photon ionization of the HOMO to a final photoelectron kinetic energy of 10 eV—is also decomposed as a linear combination along both counter-rotating directions, resulting in a time dependence for the pulse helicity. We show the field helicity for some relevant frequency components

of the optimized pulse: constant helicity  $\zeta_j(t) = \pm 1$  for frequency components not shared by both counter-rotating directions [cf. Figs. 8(a) and 8(c)] and a highly oscillatory time-profile for the frequency components simultaneously shared by both polarization directions [Figs. 8(b) and 8(d)–8(f)]. In the latter scenario, the electric field polarization direction evolves in a nontrivial fashion.

The origin of the time-delay between the right and left circularly polarized fields shown in Fig. 7 is investigated in Figs. 8(a) and 8(c), showing the temporal profile of the electric field amplitude for the subpulses with photon energies of 7.1 eV and 14.8 eV. In fact, it can be observed in Fig. 8(a) that the time at which the pulse carrying the photon energy of 7.1 eV reaches its half maximum (at  $t = 0$  fs) is precisely aligned with the peak position of the ionizing field [cf. Fig. 8(c)], which reaches its peak maximum also at  $t = 0$  fs. It can also be noted that the FWHM of the pulse in Fig. 8(a) coincides with half the overall duration of the ionizing pulse, defined by the time interval between the peak position of the ionizing pulse at  $t = 0$  fs and the time when the ionizing pulse is over ( $t \approx 42$  fs) in Fig. 8(c). As a result and under such particular conditions, the efficiency of the resonantly enhanced two-photon ionization is greatly enhanced, as the transient population of the LUMO is efficiently ionized.

Figure 9(a) (solid-red lines) shows the energy-resolved asymmetry along the optimal direction of photoelectron emission  $\theta_k^* = 135^\circ$  obtained when both optimized fields components  $\mathbf{E}_L'(t)$  and  $\mathbf{E}_R'(t - \tau)$  are simultaneously used for propagation. This scenario corresponds to the polarization-shaped case, leading to a perfect asymmetry (100%) at 10 eV. To further inspect the role of the polarization shaping, we examine the partial contribution to the total anisotropy arising from each counter-rotating component. This is performed by isolating the optimized CRP and CLP components of the overall field. Independent propagation then leads to the partial contributions. The resulting partial anisotropies are shown in blue filled circles and green empty squares in Fig. 9(a). The individual contribution from the CRP and CLP rotating components accounts for only 15% and 9%, respectively.

Remarkably, the partial contributions of each rotating component share the same sign at all angles and, in particular, at  $135^\circ$

[cf. Fig. 9(b)]. Even more remarkable is the fact that the leading contribution arises from coherent wave packet interference that originates from ionization channels driven by counter-rotating components (dotted-dashed black line), which contributes with 76% of the total asymmetry in the direction  $135^\circ$ . Such an interference term arises from the mixed terms involving the product  $\propto \mathcal{E}_{+1}' \mathcal{E}_{-1}' + cc$ . For the optimal set of parameters, the interference term does not vanish upon the orientation averaging.

The fact that both counter-rotating components independently contribute with equal sign for the anisotropy, at the optimal photoelectron energy, is also a remarkable feature resulting from the pulse shaping. In fact, the asymmetry is expected to change sign under ellipticity reversal, e.g., from CRP to CLP, provided that both rotating components have the same pulse parameters, i.e., phases and delays. However, this is not the case here. This suggests a strong interplay between the optimal phases and time delays of each counter-rotating component that are adjusted by the optimization algorithm in such a way that enforces an equal sign for the partial anisotropies obtained with each individual counter-rotating component, which further enhances the asymmetry from 76% to 100%.

Thus, the isolated contribution from both counter-rotating directions to the asymmetry amounts modestly, with 24% of the total anisotropy, while the contribution from their interference reaches 76%. Because such interferences are absent in the case of constant  $\zeta(t)$ —for which a maximal anisotropy of only 64% at 10 eV is obtained—and owing to the fact that the time-dependence of the helicity is inherently encoded in the interference term, the high degree of anisotropy is attributed to the polarization shaping of the ionizing multicolor field.

#### IV. CONCLUSIONS

We have identified two control schemes that achieve perfect anisotropy in a randomly oriented ensemble of molecules without symmetry. Bichromatic control can achieve anisotropy in the PAD even after orientational averaging; however, its efficiency to achieve perfect anisotropy was found to be limited. By extending the two-pathway control approach to a resonantly enhanced multiphoton ionization-based control formalism, we are able to recover full control of the photoelectron dynamics. The REMPI scheme involves interferences between odd-parity single-photon ionization pathway and a manifold of even-parity resonantly enhanced two-photon ionization pathways, which probe different molecular orbitals. We have shown that for linearly polarized fields, the control scheme based on multiple-REMPI outperforms bichromatic control for all photoelectron energies.

By generalizing the multiple-REMPI approach to polarization-shaped fields with time-dependent helicity, we have shown that the forward-backward anisotropy in the PAD can also be significantly enhanced. This is achieved by controlling the temporal profile of the field helicity. The control mechanism is based on interference within a manifold of photoionization pathways driven by fields with counter-rotating polarization directions. Interestingly, the isolated contributions of each optimized counter-rotating component produce only relatively moderate anisotropy. We have shown that perfect anisotropy (100%) is only achieved

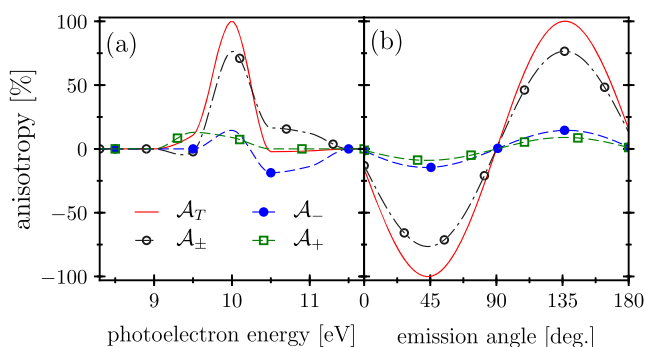


**FIG. 9.** (a) Anisotropy as a function of the photoelectron energy along the optimal direction of photoelectron emission  $\theta_k^* = 135^\circ$ . (b) Anisotropy as a function of the emission angle for the optimal photoelectron energy  $e_k^*$  of 10 eV.

when both optimized counter-rotating components are utilized simultaneously.

Nonadiabatic effects due to nuclear motion occurring at the time scales considered here may affect the resulting degree of anisotropy as the fingerprints of nonadiabatic dynamics are imprinted in the entangled nuclear-photoelectron wave packet.<sup>79,80</sup> Such nonadiabatic effects may be incorporated using standard molecular dynamics techniques, which treat the nuclear motion classically. The photoelectron wave packet and molecular orbitals would then be required to be updated accordingly, for each classical nuclear configuration. The resulting nuclear motion and subsequent hole dynamics might be used as an implicit source of control. This may be achieved by shaping pulses that would not only select the appropriate photoionization pathways but also initiate the optimal nonadiabatic dynamics to influence the entangled photoelectron wave packet in the desired manner.

With the ability to achieve perfect anisotropy in small molecules, we envision using the multiple-REMPI scheme as a sensitive probe of electron dynamics. Further design of the pulses would be advantageous, for example, to differentiate between long-lived dynamic species and multiple product channels. In this way, different measures of the anisotropy of the PADs of complex molecules can be designed to reveal their complex molecular dynamics. We also foresee extending this control procedure to more complex systems and pulse types, including those with three-photon processes.

## ACKNOWLEDGMENTS

The computing for this project was performed on the Beocat Research Cluster at Kansas State University, which is funded in part by NSF (Grant Nos. CNS-1006860, EPS-1006860, and EPS-0919443), and used resources of the National Energy Research Scientific Computing Center (NERSC), a U.S. Department of Energy Office of Science User Facility operated under Contract No. DE-AC02-05CH11231. C.P.K. acknowledges financial support from the Deutsche Forschungsgemeinschaft (Grant No. CRC 1319).

## APPENDIX A: FRAME ROTATIONS

For completeness, we provide in this section the details of the derivation of the relevant quantities involving the frame rotations presented in the text. Hartree atomic units (a.u.) are used throughout.

In the laboratory frame  $\mathcal{R}'$ , the electric field  $\mathbf{E}'(t)$  reads

$$\mathbf{E}'(t) = \sum_{\mu_0=0,\pm 1} \mathcal{E}'_{\mu_0}(t) \mathbf{e}'_{\mu_0}, \quad (\text{A1a})$$

where  $(*)$  denotes the complex conjugation and  $\mathbf{e}'_{\mu_0}$  denotes the spherical unit vectors such that

$$\mathbf{E}'(t) \cdot \mathbf{e}'_{\mu_0} = \mathcal{E}'_{\mu_0}(t). \quad (\text{A1b})$$

As stated in the text,  $\mathcal{E}'_{\mu_0}(t)$ , for  $\mu_0 = \pm 1, 0$ , refer to polarization unit components of the field in  $\mathcal{R}'$ . In this frame, the spherical unit vectors are defined in terms of their Cartesian counterparts,

$$\mathbf{e}'_{\pm} = \mp \frac{1}{\sqrt{2}} (\mathbf{e}'_x \pm \mathbf{e}'_y) \quad (\text{A1c})$$

together with  $\mathbf{e}'_0 = \mathbf{e}'_z$ . Projection of the field components into the molecular frame—which is rotated of Euler angles<sup>63,65</sup>  $\gamma_{\mathcal{R}}$  with respect to the laboratory frame—is obtained by writing the spherical unit components  $\mathbf{e}'_{\mu_0}$  in terms of their counterparts  $\mathbf{e}_{\mu_0}$  associated with the molecular frame,

$$\mathbf{e}'_{\mu_0} = \sum_{\mu=0,\pm 1} \mathcal{D}_{\mu,\mu_0}^{(1)}(\gamma_{\mathcal{R}}) \mathbf{e}_{\mu}. \quad (\text{A1d})$$

Recalling that  $\mathbf{e}_{\mu_0}^* = (-1)^{\mu_0} \mathbf{e}_{-\mu_0}$ , we find

$$\mathbf{E}(t; \gamma_{\mathcal{R}}) = \sum_{\mu,\mu_0} (-1)^{\mu_0} \mathcal{E}'_{\mu_0}(t) \mathcal{D}_{\mu,\mu_0}^{(1)}(\gamma_{\mathcal{R}}) \mathbf{e}_{\mu}, \quad (\text{A1e})$$

where  $\mathcal{D}_{\mu,\mu_0}^{(1)}(\gamma_{\mathcal{R}})$  correspond the elements of the Wigner rotation matrix.<sup>63,65</sup> Similarly, we decompose the position operator into the spherical unit basis, namely,

$$\hat{\mathbf{r}} = \sum_{\mu'=0,\pm 1} \hat{\mathbf{r}}_{\mu'} \mathbf{e}_{\mu'}^*. \quad (\text{A1f})$$

Using Eq. (A1e), the molecular-frame orientation-dependent dipole interaction reads

$$\mathbf{E}(t; \gamma_{\mathcal{R}}) \cdot \hat{\mathbf{r}} = \sum_{\mu_0} (-1)^{\mu_0} \mathcal{E}'_{\mu_0}(t) \sum_{\mu} \mathcal{D}_{\mu,-\mu_0}^{(1)}(\gamma_{\mathcal{R}}) \hat{\mathbf{r}}_{\mu}, \quad (\text{A1g})$$

which corresponds to the dipole interaction in the molecular frame  $\mathcal{R}$  given in Eq. (2b) in the text.

A second kind of rotation operations involves projection of the direction of photoelectron emission from the molecular to the laboratory frame coordinates as defined in Eq. (13b). This results in the expressions for the first and second order corrections in the laboratory frame of reference outlined in Eqs. (14) and (15), respectively. However, instead of calculating  $\alpha_{i_0}^{k(n)}(t; \gamma_{\mathcal{R}}) \cdot \alpha_{i_0}^{k'(m)*}(t; \gamma_{\mathcal{R}})$ , directly from Eqs. (14) and (15), it turns out to be more convenient to rotate the anisotropy parameters themselves instead of calculating the anisotropy parameters from the rotated expansion coefficients. Specifically, we follow the prescription:

- (a) Keep the ionization amplitudes  $\alpha_{i_0}^{k(n)}(t; \gamma_{\mathcal{R}})$ , in the molecular frame, defined by

$$\alpha_{i_0}^{k(1)}(t; \gamma_{\mathcal{R}}) = i \sum_{\mu_0,\mu} (-1)^{\mu_0} \sum_{\ell,m} \mathcal{D}_{\mu,-\mu_0}^{(1)}(\gamma_{\mathcal{R}}) (\mathbf{r}_{k,\ell,m;i_0} \cdot \mathbf{e}_{\mu}) Y_{\ell}^m(\theta_k, \phi_k) \int_{-\infty}^t e^{-i(\epsilon_0 - \epsilon_{i_0}^k)} \mathcal{E}'_{\mu_0}(t') dt', \quad (\text{A2a})$$

for first order processes, and

$$\alpha_{i_0}^{k(2)}(t; \gamma_{\mathcal{R}}) = - \sum_{\mu_0, \nu_0} (-1)^{\mu_0 + \nu_0} \sum_{\mu, \nu} \mathcal{D}_{\mu, -\mu_0}^{(1)}(\gamma_{\mathcal{R}}) \mathcal{D}_{\nu, -\nu_0}^{(1)}(\gamma_{\mathcal{R}}) \sum_{\ell, m} Y_{m'}^{\ell}(\theta_k, \phi_k) \left[ (\mathbf{r}_{k, \ell, m; i_0} \cdot \mathbf{e}_{\mu}) \sum_i (\mathbf{r}_{i, i} \cdot \mathbf{e}_{\nu}) \int_{-\infty}^t e^{-i(\epsilon_{i_0} - \epsilon_k)t'} \mathcal{E}_{\mu_0}^{\nu}(t') \right. \\ \left. \times \int_{-\infty}^{t'} \mathcal{E}_{\nu_0}^{\mu}(t'') dt'' dt' + \sum_b (\mathbf{r}_{k, \ell, m; b} \cdot \mathbf{e}_{\mu}) (\mathbf{r}_{b, i_0} \cdot \mathbf{e}_{\nu}) \int_{-\infty}^t e^{-i(\epsilon_b - \epsilon_k)t'} \mathcal{E}_{\mu_0}^{\nu}(t') \int_{-\infty}^{t'} e^{-i(\epsilon_{i_0} - \epsilon_b)t''} \mathcal{E}_{\nu_0}^{\mu}(t'') dt'' dt' \right], \quad (\text{A2b})$$

for second order processes. For reasons that will become clearer later, we seek to express the products  $\alpha_{i_0}^{k(n)}(t; \gamma_{\mathcal{R}})$   $\alpha_{i_0}^{k(m)*}(t; \gamma_{\mathcal{R}})$  in terms of a product involving three Wigner rotation matrices. To this end, it is convenient to express the product  $\mathcal{D}_{\mu, -\mu_0}^{(1)}(\gamma_{\mathcal{R}}) \mathcal{D}_{\nu, -\nu_0}^{(1)}(\gamma_{\mathcal{R}})$  in Eq. (A2b) in terms of its irreducible representation using the elementary expression<sup>63,65</sup>

$$\mathcal{D}_{m_1, m_1'}^{(\ell_1)}(\gamma_{\mathcal{R}}) \mathcal{D}_{m_2, m_2'}^{(\ell_2)}(\gamma_{\mathcal{R}}) = \sum_{\ell} (2\ell + 1) \mathcal{D}_{-m_{12}, -m_{12}'}^{*(\ell)}(\gamma_{\mathcal{R}}) \\ \times \begin{pmatrix} \ell_1 & \ell_2 & \ell \\ m_1 & m_2 & -m_{12} \end{pmatrix} \\ \times \begin{pmatrix} \ell_1 & \ell_2 & \ell \\ m_1' & m_2' & -m_{12}' \end{pmatrix},$$

with  $m_{12} = m_1 + m_2$  and  $m_{12}' = m_1' + m_2'$ .

- (b) When calculating  $\alpha_{i_0}^{k(n)}(t; \gamma_{\mathcal{R}}) \alpha_{i_0}^{k(m)*}(t; \gamma_{\mathcal{R}})$  a product involving the spherical harmonics,  $Y_{m'}^{\ell}(\theta_k, \phi_k) Y_{m'}^{\ell'*}(\theta_k, \phi_k)$  appears. The strategy is to first express such a product in terms of its irreducible representation, namely,

$$Y_m^{\ell}(\Omega_k) Y_{m'}^{\ell'*}(\Omega_k) = (-1)^{m'} \sum_{L=|\ell-\ell'|}^{\ell+\ell'} \eta_{\ell, \ell'}^L Y_{m-m'}^{L*}(\Omega_k) \\ \times \begin{pmatrix} \ell & \ell' & L \\ 0 & 0 & 0 \end{pmatrix} \begin{pmatrix} \ell & \ell' & L \\ m & -m' & m' - m \end{pmatrix}, \quad (\text{A3})$$

with  $\eta_{\ell, \ell'}^L = \sqrt{(2\ell+1)(2\ell'+1)/4\pi}$  and where we have defined  $\Omega_{k'} = (\theta_{k'}, \phi_{k'})$ .

- (c) Next, we rotate the resulting spherical harmonic in Eq. (A3) in the laboratory frame,  $\mathcal{R}'$ , using the inverse of the frame transformation defined in Eq. (A1d), namely,

$$Y_{m-m'}^L(\Omega_k) = \sum_{M=-L}^L \mathcal{D}_{M, m-m'}^{(1)\dagger}(\gamma_{\mathcal{R}}) Y_M^L(\Omega_{k'}). \quad (\text{A4})$$

- (d) Finally, we write  $Y_M^L(\Omega_{k'})$  in Eq. (A4) in terms of the associated Legendre polynomials<sup>63,65</sup>

$$Y_M^L(\Omega_{k'}) = (-1)^M \sqrt{\frac{(2L+1)(L-M)!}{4\pi(L+M)!}} P_L^M(\cos \theta_{k'}) e^{iM\phi_{k'}}. \quad (\text{A5})$$

- (e) Following these steps, Eq. (A3) finally reads

$$Y_{m'}^{\ell}(\theta_k, \phi_k) Y_{m'}^{\ell'*}(\theta_k, \phi_k) \\ = (-1)^{m'} \sum_{L=|\ell-\ell'|}^{\ell+\ell'} \frac{2L+1}{4\pi} \sqrt{(2\ell+1)(2\ell'+1)} \begin{pmatrix} \ell & \ell' & L \\ 0 & 0 & 0 \end{pmatrix} \\ \times \begin{pmatrix} \ell & \ell' & L \\ m & -m' & m' - m \end{pmatrix} \sum_{M=-L}^L \sqrt{\frac{(L-M)!}{(L+M)!}} \\ \times \mathcal{D}_{m'-m, -M}^{(L)}(\gamma_{\mathcal{R}}) P_L^M(\cos \theta_{k'}) e^{iM\phi_{k'}}, \quad (\text{A6})$$

which transforms the anisotropy parameters from the molecular to the laboratory frame of reference. Thus, this strategy is equivalent to rotate the anisotropy parameters instead of performing the full derivation using the rotated wave function coefficients. Apart from significantly reducing the number of operations in the summations when calculating the norm squared of first and second order corrections, it has the advantage of leading to an expression for  $M = -L$ ,  $L$  in  $\beta_{L, M}^{(\cdot)}(\epsilon_k)$ , as a function of the polarization unit vectors  $\epsilon_{\mu_0}, \epsilon_{\nu_0}$  and  $\epsilon_{\mu_0'}, \epsilon_{\nu_0}'$  in a straightforward manner, which facilitates the analysis of the selection rules for the anisotropy as a function of the field polarization direction.

## APPENDIX B: ORIENTATION-AVERAGED ANISOTROPY PARAMETERS

### 1. Anisotropy parameters $\beta_{L, M}^{1ph}$

Following the guidelines for rotating the anisotropy parameters introduced in Appendix A, the orientation-averaged ionization probability distribution for one-photon ionization measured in the laboratory frame,  $\mathcal{R}'$ , is obtained upon rotation of  $|\alpha_{i_0}^{k(1)}(t; \gamma_{\mathcal{R}})|^2$ —using Eq. (A2a)—from the molecular to the laboratory frame or reference, and integrating over all Euler angles  $\gamma_{\mathcal{R}}$ . We find

$$|\alpha_{i_0}^{k(1)}(\gamma_{\mathcal{R}})|^2 = \sum_{L, M} \frac{(2L+1)}{4\pi} \sqrt{\frac{(L-M)!}{(L+M)!}} \sum_{\mu_0} (-1)^{-\mu_0} \mathcal{I}_{\mu_0}(k, t) \sum_{\mu_0'} \mathcal{I}_{\mu_0'}^*(k, t) \sum_{\ell, m, \mu} (\mathbf{r}_{k, \ell, m; i_0} \cdot \mathbf{e}_{\mu}) \sum_{\ell', m', \mu'} (\mathbf{r}_{k, \ell', m'; i_0}^* \cdot \mathbf{e}_{\mu'}) (-1)^{\mu'+m'} \sqrt{(2\ell+1)(2\ell'+1)} \\ \times \begin{pmatrix} \ell & \ell' & L \\ 0 & 0 & 0 \end{pmatrix} \begin{pmatrix} \ell & \ell' & L \\ m & -m' & m' - m \end{pmatrix} P_L^M(\cos \theta_{k'}) e^{+iM\phi_{k'}} \int \frac{d^3\gamma_{\mathcal{R}}}{8\pi^2} \mathcal{D}_{\mu, -\mu_0}^{(1)}(\gamma_{\mathcal{R}}) \mathcal{D}_{-\mu', \mu_0'}^{(1)}(\gamma_{\mathcal{R}}) \mathcal{D}_{m'-m, -M}^{(L)}(\gamma_{\mathcal{R}}) \quad (\text{B1})$$

for  $t \rightarrow \infty$  and where we have defined

$$\mathcal{I}_{\mu_0}(k, t) = \int_{-\infty}^t \mathcal{E}_{\mu_0}'(t') e^{i(\epsilon_k - \epsilon_{i_0})t'} dt'. \quad (\text{B2})$$

Integration of Eq. (B1) over the Euler angles defines, according to Eq. (9), the laboratory-frame orientation-averaged anisotropy parameter  $\beta_{L,M}^{(\mu_0)1ph}(\epsilon_k)$  corresponding to the first order process. Integration of a product involving three Wigner  $3j$ - symbols can be

performed analytically,<sup>63,65</sup>

$$\int \mathcal{D}_{m_1, m_1'}^{(\ell_1)}(\gamma_{\mathcal{R}}) \mathcal{D}_{m_2, m_2'}^{(\ell_2)}(\gamma_{\mathcal{R}}) \mathcal{D}_{m_3, m_3'}^{(\ell_3)}(\gamma_{\mathcal{R}}) \frac{d^3 \gamma_{\mathcal{R}}}{8\pi^2} = \begin{pmatrix} \ell_1 & \ell_2 & \ell_3 \\ m_1 & m_2 & m_3 \end{pmatrix} \begin{pmatrix} \ell_1 & \ell_2 & \ell_3 \\ m_1' & m_2' & m_3' \end{pmatrix}, \quad (\text{B3})$$

which gives, upon equating Eqs. (9) and (B1), the final expression,

$$\beta_{L,M}^{1ph}(\epsilon_k) = \frac{(2L+1)}{4\pi} \sqrt{\frac{(L-M)!}{(L+M)!}} \sum_{\mu_0} (-1)^{-\mu_0} \mathcal{I}_{\mu_0}(k, t) \sum_{\mu'_0} \mathcal{I}_{\mu'_0}^*(k, t) \sum_{\ell, m, \mu} (\mathbf{r}_{k, \ell, m; i_0} \cdot \mathbf{e}_{\mu}) \sum_{\ell', m', \mu'} (\mathbf{r}_{k, \ell', m'; i_0} \cdot \mathbf{e}_{\mu'})^* (-1)^{\mu'+m'} \sqrt{(2\ell+1)(2\ell'+1)} \times \begin{pmatrix} \ell & \ell' & L \\ 0 & 0 & 0 \end{pmatrix} \begin{pmatrix} \ell & \ell' & L \\ m & -m' & m' - m \end{pmatrix} \begin{pmatrix} 1 & 1 & L \\ \mu & -\mu' & m' - m \end{pmatrix} \begin{pmatrix} 1 & 1 & L \\ -\mu_0 & \mu'_0 & -M \end{pmatrix}, \quad (\text{B4})$$

which corresponds to the quantity displayed in Eq. (16a) in the text.

## 2. Anisotropy parameters $\beta_{L,M}^{2ph}$

To evaluate the laboratory-frame orientation-averaged anisotropy parameters describing the contribution from second

order processes,  $\beta_{L,M}^{2ph}(\epsilon_k)$ , we employ the same strategy involving the elementary angular momentum algebra detailed in Sec. B 1. Using Eq. (A2b) and upon evaluation of the product  $\alpha_{B_0}^{k(2)}(\epsilon_k) \cdot \alpha_{B_0}^{k(2)*}(\epsilon_k)$ , followed by projection of quantity into the laboratory frame coordinates as indicated above, we find, with the help of Eq. (9),

$$\beta_{L,M}^{2ph}(\epsilon_k) = \frac{(2L+1)}{4\pi} \sqrt{\frac{(L-M)!}{(L+M)!}} \sum_{\mu_0, \nu_0} \sum_{\mu, \nu} (-1)^{-\mu-\nu} \sum_{Q_1=0}^2 g_{\mu, \nu, \mu_0, \nu_0}^{(Q_1)} \sum_{\mu'_0, \nu'_0} \sum_{\mu', \nu'} (-1)^{\mu'_0+\nu'_0} \sum_{Q_2=0}^2 g_{\mu', \nu', \mu'_0, \nu'_0}^{(Q_2)} \times \sum_{\ell, m} \sum_{\ell', m'} (-1)^{m'} \sqrt{(2\ell+1)(2\ell'+1)} \sum_{p, p' \geq i_0} \mathcal{S}_{\mu', \nu'}^{p' *} (k, \ell', m') \mathcal{F}_{\mu'_0, \nu'_0}^{p' *} (t; k) \mathcal{S}_{\mu, \nu}^p (k, \ell, m) \mathcal{F}_{\mu_0, \nu_0}^p (t; k) \times \begin{pmatrix} \ell & \ell' & L \\ 0 & 0 & 0 \end{pmatrix} \begin{pmatrix} \ell & \ell' & L \\ m & -m' & m' - m \end{pmatrix} \begin{pmatrix} Q_1 & Q_2 & L \\ \mu + \nu & -\mu' - \nu' & m' - m \end{pmatrix} \begin{pmatrix} Q_1 & Q_2 & L \\ -\mu_0 - \nu_0 & \mu'_0 + \nu'_0 & -M \end{pmatrix}. \quad (\text{B5})$$

Note that the limits on the sum over  $Q_1$  and  $Q_2$  imply that the two-photon processes contribute with a polynomial order of  $L = 4$  at the most. In Eq. (16b), we have defined

$$g_{\mu, \mu', \mu'_0, \nu'_0}^{(Q)} \equiv c_Q \begin{pmatrix} 1 & 1 & Q \\ \mu & \nu & -\mu - \nu \end{pmatrix} \begin{pmatrix} 1 & 1 & Q \\ -\mu_0 & -\nu_0 & \mu_0 + \nu_0 \end{pmatrix}, \quad (\text{B6a})$$

with  $c_Q = (2Q + 1)$ . The term  $\mathcal{F}_{\mu_0, \nu_0}^p(t; k)$  in Eq. (B5) is given by

$$\mathcal{F}_{\mu_0, \nu_0}^p(t; k) = \int_{-\infty}^t e^{i(\epsilon_k - \epsilon_p)t'} \mathcal{E}_{\mu_0}'(t') \int_{-\infty}^{t'} e^{i(\epsilon_p - \epsilon_{i_0})t''} \mathcal{E}_{\nu_0}'(t'') dt' dt''. \quad (\text{B6b})$$

Finally, the term  $\mathcal{S}_{\mu, \nu}^p(k, \ell, m)$  in Eq. (B5) reads

$$\mathcal{S}_{\mu, \nu}^p(k, \ell, m) = (1 - \delta_{p, i_0}) (\mathbf{r}_{k, \ell, m; p} \cdot \mathbf{e}_{\mu}) (\mathbf{r}_{p, i_0} \cdot \mathbf{e}_{\nu}) + \delta_{p, i_0} \sum_{i \in occ} (\mathbf{r}_{k, \ell, m; p} \cdot \mathbf{e}_{\mu}) (\mathbf{r}_{i, i} \cdot \mathbf{e}_{\nu}) \quad (\text{B6c})$$

for  $p \geq i_0$ . From Eq. (B6a) and the fourth Wigner  $3j$ -symbol in Eq. (B5), it follows that second-order processes also lead to vanishing asymmetries in the PAD for linearly polarized fields. In fact, Eq. (B6a) vanishes for  $Q$  odd, while the fourth Wigner  $3j$ -symbol Eq. (16b) requires  $Q_1 + Q_2$  to be odd for  $L$  odd.

### 3. Anisotropy parameters $\beta_{L,M}^{int}$

The contribution to the photoelectron momentum distribution originating from the interference between single- and two-photon pathways is obtained using the same strategy employed in Secs. B 1 and B 2. Upon straightforward angular momentum algebra, we find

$$\begin{aligned} \beta_{L,M}^{int}(\epsilon_k) = & -i \frac{(2L+1)}{4\pi} \sqrt{\frac{(L-M)!}{(L+M)!}} \sum_{\mu, \ell, m; i_0} (\mathbf{r}_{k, \ell, m; i_0} \cdot \mathbf{e}_\mu) \sum_{\mu_0} (-1)^{-\mu_0} \int_{-\infty}^t \mathcal{E}_{\mu_0}^{\prime}(t') e^{+(\epsilon_k - \epsilon_{i_0})t'} dt' \\ & \times \sum_{\mu'_0, \nu'_0} (-1)^{\mu'_0 + \nu'_0} \sum_{\mu', \nu'} \sum_{Q_2=0}^2 g_{\mu', \nu'; \mu'_0, \nu'_0}^{(Q_2)} \sum_{\ell', m'} (-1)^{m'} \sum_{p \geq i_0} \mathcal{S}_{\mu', \nu'}^{p' *} (k, \ell', m') \mathcal{F}_{\mu'_0, \nu'_0}^{p' *} (t; k) \\ & \times \sqrt{(2\ell+1)(2\ell'+1)} \begin{pmatrix} \ell & \ell' & L \\ 0 & 0 & 0 \end{pmatrix} \begin{pmatrix} \ell & \ell' & L \\ m & -m' & m' - m \end{pmatrix} \begin{pmatrix} 1 & Q_2 & L \\ \mu & -\mu' - \nu' & m' - m \end{pmatrix} \begin{pmatrix} 1 & Q_2 & L \\ -\mu_0 & \mu'_0 + \nu'_0 & -M \end{pmatrix} \end{aligned} \quad (B7)$$

for  $t \rightarrow \infty$  and where the terms  $g_{\mu', \nu'; \mu'_0, \nu'_0}^{(Q_2)}$ ,  $\mathcal{S}_{\mu', \nu'}^{p' *} (k, \ell', m')$ , and  $\mathcal{F}_{\mu'_0, \nu'_0}^{p' *} (t; k)$  in Eq. (B7) are given in Eqs. (B6a)–(B6b), respectively.

From the third and fourth Wigner 3j-symbols in Eq. (B7), it is apparent that the interference term  $\beta_{L,M}^{int}$  may contribute to the anisotropy after the orientation-averaging, even for linearly polarized fields. In fact, for  $L$  odd and  $Q_2$  even, both symbols do not necessarily vanish by selection rules, in contrast to  $\beta_{L,M}^{1ph}$  and  $\beta_{L,M}^{2ph}$ . Conversely, for circularly polarized fields, or fields with unequal counter-rotating components, all three orientation-averaged anisotropy parameters may contribute to the anisotropy in the photoelectron emission in the case of a chiral target. For achiral targets, only interference term can be used to break the asymmetry.

### APPENDIX C: PULSE PARAMETERIZATION FOR POLARIZATION SHAPED PULSES

For polarization shaped pulses, we consider a superposition of pulses with different counter-rotating components, namely,

$$\mathbf{E}'(t) = \mathbf{E}'_R(t) + \mathbf{E}'_L(t). \quad (C1a)$$

Each rotating component, carrying circularly left and right polarization,  $\mathbf{E}'_{L,R}(t)$ , is projected into the polarization unit vectors,  $\mathbf{e}'_{\pm}$ , according to

$$\mathbf{E}'_{L,R}(t) = \mathcal{E}'_{+}{}^{L,R}(t) \mathbf{e}'_{+1} + \mathcal{E}'_{-}{}^{L,R}(t) \mathbf{e}'_{-1}, \quad (C1b)$$

where the CRP and CLP components  $\mathcal{E}'_{\pm}{}^{L,R} = \mathbf{E}'_{L,R} \cdot \mathbf{e}'_{\pm}$  are (independently) parameterized according to

$$\mathcal{E}'_{\pm}{}^{L,R}(t) = \pm \frac{1}{\sqrt{2}} \sum_{j=1}^N h_j(t - \tau_j) e^{\pm i\omega_j(t - \tau_j) + \phi_j} \quad (C1c)$$

for circularly right polarization (CRP). Its counter-rotating counterpart takes the form

$$\mathcal{E}'_{\pm}{}^{L,R}(t) = \mp \frac{1}{\sqrt{2}} \sum_{j=1}^N h_j(t - \tau_j) e^{\mp i\omega_j(t - \tau_j) + \phi_j}, \quad (C1d)$$

which allows us to retrieve the rotating field components in Cartesian coordinates

$$\mathbf{E}'_{L,R} = \sum_{j=1}^N h(t - \tau_j) \begin{pmatrix} \pm \cos \Omega_j(t) \\ -\sin \Omega_j(t) \\ 0 \end{pmatrix} \quad (C1e)$$

for circularly right (–) and left (+) polarization directions from the source point of view in the laboratory frame of reference and where  $\Omega_j(t) = \omega_j(t - \tau_j) + \phi_j$ . The pulse parameters in Eqs. (C1c) and (C1d) are independently optimized for both counter-rotating components.

### REFERENCES

- <sup>1</sup>E. Allaria, R. Appio, L. Badano, W. Barletta, S. Bassanese, S. Biedron, A. Borgia, E. Busetto, D. Castronovo, P. Cinquegrana *et al.*, *Nat. Photonics* **6**, 699 (2012).
- <sup>2</sup>C. Spezzani, E. Allaria, M. Coreno, B. Diviacco, E. Ferrari, G. Geloni, E. Karantzoulis, B. Mahieu, M. Vento, and G. De Nino, *Phys. Rev. Lett.* **107**, 084801 (2011).
- <sup>3</sup>B. Brehm and E. von Puttkamer, *Z. Naturforsch., A* **22**, 8 (1967).
- <sup>4</sup>T. Baer, J. Booze, and K.-M. Weitzel, *Vacuum Ultraviolet Photoionization and Photodissociation of Molecules and Clusters* (World Scientific, 1991), pp. 259–296.
- <sup>5</sup>A. Bodi, M. Johnson, T. Gerber, Z. Gengeliczki, B. Sztáray, and T. Baer, *Rev. Sci. Instrum.* **80**, 034101 (2009).
- <sup>6</sup>D. Normand, L. Lompre, and C. Cornaggia, *J. Phys. B: At., Mol. Opt. Phys.* **25**, L497 (1992).
- <sup>7</sup>H. Stapelfeldt, *Phys. Scr.* **110**, 132 (2004).
- <sup>8</sup>C. Horn, M. Wollenhaupt, M. Krug, T. Baumert, R. De Nalda, and L. Banares, *Phys. Rev. A* **73**, 031401 (2006).
- <sup>9</sup>I. Powis, *Adv. Chem. Phys.* **138**, 267 (2008).
- <sup>10</sup>N. Böwering, T. Lischke, B. Schmidtke, N. Müller, T. Khalil, and U. Heinzmann, *Phys. Rev. Lett.* **86**, 1187 (2001).
- <sup>11</sup>L. Nahon, G. A. Garcia, C. J. Harding, E. Mikajlo, and I. Powis, *J. Chem. Phys.* **125**, 114309 (2006).
- <sup>12</sup>C. J. Harding, E. Mikajlo, I. Powis, S. Barth, S. Joshi, V. Ulrich, and U. Hergenhahn, *J. Chem. Phys.* **123**, 234310 (2005).
- <sup>13</sup>C. Lux, M. Wollenhaupt, C. Sarpe, and T. Baumert, *ChemPhysChem* **16**, 115 (2015).
- <sup>14</sup>K.-J. Yuan and A. D. Bandrauk, *J. Mod. Opt.* **60**, 1492 (2013).
- <sup>15</sup>Y.-Y. Yin, D. Elliott, R. Shehadeh, and E. Grant, *Chem. Phys. Lett.* **241**, 591 (1995).
- <sup>16</sup>N. Douguet, A. N. Grum-Grzhimailo, E. V. Gryzlova, E. I. Staroselskaya, J. Venzke, and K. Bartschat, *Phys. Rev. A* **93**, 033402 (2016).

- <sup>17</sup>A. Grum-Grzhimailo, E. Gryzlova, E. Staroselskaya, S. Strakhova, J. Venzke, N. Douguet, and K. Bartschat, *J. Phys.: Conf. Ser.* **635**, 012008 (2015).
- <sup>18</sup>N. Douguet, A. N. Grum-Grzhimailo, and K. Bartschat, *Phys. Rev. A* **95**, 013407 (2017).
- <sup>19</sup>E. Gryzlova, A. Grum-Grzhimailo, E. Staroselskaya, N. Douguet, and K. Bartschat, *Phys. Rev. A* **97**, 013420 (2018).
- <sup>20</sup>K.-J. Yuan and A. D. Bandrauk, *J. Phys. B: At., Mol. Opt. Phys.* **49**, 065601 (2016).
- <sup>21</sup>W. Hu, Y. Liu, S. Luo, X. Li, J. Yu, X. Li, Z. Sun, K.-J. Yuan, A. D. Bandrauk, and D. Ding, *Phys. Rev. A* **99**, 011402 (2019).
- <sup>22</sup>K.-J. Yuan, S. Chelkowski, and A. D. Bandrauk, *Phys. Rev. A* **93**, 053425 (2016).
- <sup>23</sup>P. V. Demekhin, A. N. Artemyev, A. Kastner, and T. Baumert, e-print [arXiv:1807.01097](https://arxiv.org/abs/1807.01097) (2018).
- <sup>24</sup>P. V. Demekhin, A. N. Artemyev, A. Kastner, and T. Baumert, *Phys. Rev. Lett.* **121**(25), 253201 (2018).
- <sup>25</sup>C. S. Lehmann, N. B. Ram, I. Powis, and M. H. M. Janssen, *J. Chem. Phys.* **139**, 234307 (2013).
- <sup>26</sup>M. H. M. Janssen and I. Powis, *Phys. Chem. Chem. Phys.* **16**, 856 (2014).
- <sup>27</sup>M. M. R. Fanoood, N. B. Ram, C. S. Lehmann, I. Powis, and M. H. M. Janssen, *Nat. Commun.* **6**, 7511 (2015).
- <sup>28</sup>M. M. R. Fanoood, M. H. M. Janssen, and I. Powis, *Phys. Chem. Chem. Phys.* **17**, 8614 (2015).
- <sup>29</sup>F. Rafiee, M. Mohammad, M. H. M. Janssen, and I. Powis, *J. Chem. Phys.* **145**(12), 124320 (2016).
- <sup>30</sup>S. Beaulieu, A. Comby, D. Descamps, B. Fabre, G. Garcia, R. Géneaux, A. Harvey, F. Légaré, Z. Mašín, L. Nahon *et al.*, *Nat. Phys.* **14**, 484 (2018).
- <sup>31</sup>S. Beaulieu, A. Ferré, R. Géneaux, R. Canonge, D. Descamps, B. Fabre, N. Fedorov, F. Légaré, S. Petit, T. Ruchon *et al.*, *New J. Phys.* **18**, 102002 (2016).
- <sup>32</sup>A. Kastner, C. Lux, T. Ring, S. Züllighoven, C. Sarpe, A. Senftleben, and T. Baumert, *ChemPhysChem* **17**, 1119 (2016).
- <sup>33</sup>J. Miles, D. Fernandes, A. Young, C. Bond, S. Crane, O. Ghafur, D. Townsend, J. Sá, and J. Greenwood, *Anal. Chim. Acta* **984**, 134 (2017).
- <sup>34</sup>A. Comby, S. Beaulieu, M. Boggio-Pasqua, D. Descamps, F. Légaré, L. Nahon, S. Petit, B. Pons, B. Fabre, Y. Mairesse *et al.*, *J. Phys. Chem. Lett.* **7**, 4514 (2016).
- <sup>35</sup>S. Beaulieu, A. Comby, B. Fabre, D. Descamps, A. Ferré, G. Garcia, R. Géneaux, F. Légaré, L. Nahon, S. Petit *et al.*, *Faraday Discuss.* **194**, 325 (2016).
- <sup>36</sup>M. Shapiro and P. Brumer, *Quantum Control of Molecular Processes* (John Wiley & Sons, 2012).
- <sup>37</sup>H. G. Muller, P. H. Bucksbaum, D. W. Schumacher, and A. Zavriyev, *J. Phys. B: At., Mol. Opt. Phys.* **23**, 2761 (1990).
- <sup>38</sup>Y.-Y. Yin, C. Chen, D. S. Elliott, and A. V. Smith, *Phys. Rev. Lett.* **69**, 2353 (1992).
- <sup>39</sup>D. W. Schumacher, F. Weihe, H. G. Muller, and P. H. Bucksbaum, *Phys. Rev. Lett.* **73**, 1344 (1994).
- <sup>40</sup>A. N. Grum-Grzhimailo, E. V. Gryzlova, E. I. Staroselskaya, J. Venzke, and K. Bartschat, *Phys. Rev. A* **91**, 063418 (2015).
- <sup>41</sup>J. G. Underwood and K. L. Reid, *J. Chem. Phys.* **113**, 1067 (2000).
- <sup>42</sup>Y.-i. Suzuki and T. Seideman, *J. Chem. Phys.* **122**, 234302 (2005).
- <sup>43</sup>S.-K. Son, S.-I. Chu *et al.*, *Phys. Rev. A* **80**, 011403 (2009).
- <sup>44</sup>P. Hockett, *New J. Phys.* **17**, 023069 (2015).
- <sup>45</sup>A. N. Artemyev, A. D. Müller, D. Hochstuhl, and P. V. Demekhin, *J. Chem. Phys.* **142**, 244105 (2015).
- <sup>46</sup>B. Ritchie, *Phys. Rev. A* **13**, 1411 (1976).
- <sup>47</sup>N. Chandra, *Phys. Rev. A* **36**, 3163 (1987).
- <sup>48</sup>N. Chandra, *J. Phys. B: At. Mol. Phys.* **20**, 3405 (1987).
- <sup>49</sup>R. E. Goetz, T. A. Isaev, B. Nikoobakht, R. Berger, and C. P. Koch, *J. Chem. Phys.* **146**, 024306 (2017).
- <sup>50</sup>S. Beaulieu, A. Comby, D. Descamps, S. Petit, F. Légaré, B. Fabre, V. Blanchet, and Y. Mairesse, *J. Chem. Phys.* **149**, 134301 (2018).
- <sup>51</sup>I. Dreissigacker and M. Lein, *Phys. Rev. A* **89**, 053406 (2014).
- <sup>52</sup>K. Misawa, *Adv. Phys.: X* **1**, 544 (2016).
- <sup>53</sup>T. Brixner and G. Gerber, *Opt. Lett.* **26**, 557 (2001).
- <sup>54</sup>T. Brixner, G. Krampert, P. Niklaus, and G. Gerber, *Appl. Phys. B* **74**, s133 (2002).
- <sup>55</sup>T. Brixner, G. Krampert, T. Pfeifer, R. Selle, G. Gerber, M. Wollenhaupt, O. Graefe, C. Horn, D. Liese, and T. Baumert, *Phys. Rev. Lett.* **92**, 208301 (2004).
- <sup>56</sup>M. Plewicky, F. Weise, S. M. Weber, and A. Lindinger, *Appl. Opt.* **45**, 8354 (2006).
- <sup>57</sup>R. Selle, P. Nuernberger, F. Langhojer, F. Dimler, S. Fechner, G. Gerber, and T. Brixner, *Opt. Lett.* **33**, 803 (2008).
- <sup>58</sup>M. Ninck, A. Galler, T. Feurer, and T. Brixner, *Opt. Lett.* **32**, 3379 (2007).
- <sup>59</sup>P. Hockett, M. Wollenhaupt, and T. Baumert, *J. Phys. B: At., Mol. Opt. Phys.* **48**, 214004 (2015).
- <sup>60</sup>S. Kerbstadt, D. Pengel, D. Johannmeyer, L. Englert, T. Bayer, and M. Wollenhaupt, *New J. Phys.* **19**, 103017 (2017).
- <sup>61</sup>D. Tannor and S. Rice, *J. Chem. Phys.* **83**, 5013 (1985).
- <sup>62</sup>S. J. Glaser, U. Boscain, T. Calarco, C. P. Koch, W. Köckenberger, R. Kosloff, I. Kuprov, B. Luy, S. Schirmer, T. Schulte-Herbrüggen, D. Sugny, and F. K. Wilhelm, *Eur. Phys. J. D* **69**, 279 (2015).
- <sup>63</sup>A. R. Edmonds, *Angular Momentum in Quantum Mechanics* (Princeton University Press, 2016).
- <sup>64</sup>L. Greenman, P. J. Ho, S. Pabst, E. Kamarchik, D. A. Mazziotti, and R. Santra, *Phys. Rev. A* **82**, 023406 (2010).
- <sup>65</sup>M. Rose, Inc., *Elementary Theory of Angular Momentum* (M. Rose, Inc., New York, 1957).
- <sup>66</sup>T. Klamroth, *Phys. Rev. B* **68**, 245421 (2003).
- <sup>67</sup>H.-J. Werner, P. J. Knowles, G. Knizia, F. R. Manby, M. Schütz, P. Celani, T. Korona, R. Lindh, A. Mitrushenkov, G. Rauhut, K. R. Shamasundar, T. B. Adler, R. D. Amos, A. Bernhardsson, A. Berning, D. L. Cooper, M. J. O. Deegan, A. J. Dobbyn, F. Eckert, E. Goll, C. Hampel, A. Hesselmann, G. Hetzer, T. Hrenar, G. Jansen, C. Köppl, Y. Liu, A. W. Lloyd, R. A. Mata, A. J. May, S. J. McNicholas, W. Meyer, M. E. Mura, A. Nicklass, D. P. O'Neill, P. Palmieri, D. Peng, K. Pflüger, R. Pitzer, M. Reiher, T. Shiozaki, H. Stoll, A. J. Stone, R. Tarroni, T. Thorsteinsson, and M. Wang, *MOLPRO*, version 2012.1, a package of *ab initio* programs, 2012, see <http://www.molpro.net>.
- <sup>68</sup>H.-J. Werner, P. J. Knowles, G. Knizia, F. R. Manby, and M. Schütz, *Wiley Interdiscip. Rev.: Comput. Mol. Sci.* **2**, 242 (2012).
- <sup>69</sup>R. A. Kendall, T. H. Dunning, Jr., and R. J. Harrison, *J. Chem. Phys.* **96**, 6796 (1992).
- <sup>70</sup>R. R. Lucchese, K. Takatsuka, and V. McKoy, *Phys. Rep.* **131**, 147 (1986).
- <sup>71</sup>K. L. Reid, *Annu. Rev. Phys. Chem.* **54**, 397 (2003).
- <sup>72</sup>F. A. Gianturco, R. R. Lucchese, and N. Sanna, *J. Chem. Phys.* **100**, 6464 (1994).
- <sup>73</sup>A. P. P. Natalense and R. R. Lucchese, *J. Chem. Phys.* **111**, 5344 (1999).
- <sup>74</sup>L. Greenman, R. R. Lucchese, and C. W. McCurdy, *Phys. Rev. A* **96**, 052706 (2017).
- <sup>75</sup>M. Baertschy, T. N. Rescigno, and C. W. McCurdy, *Phys. Rev. A* **64**, 022709 (2001).
- <sup>76</sup>W. H. Miller and B. M. D. D. Jansen op de Haar, *J. Chem. Phys.* **86**, 6213 (1987).
- <sup>77</sup>B. D. Guenther, *Modern Optics* (Wiley, 1990).
- <sup>78</sup>R. E. Goetz, M. Merkel, A. Karamatskou, R. Santra, and C. P. Koch, *Phys. Rev. A* **94**, 023420 (2016).
- <sup>79</sup>M. Kowalewski, K. Bennett, J. R. Rouxel, and S. Mukamel, *Phys. Rev. Lett.* **117**, 043201 (2016).
- <sup>80</sup>L. Cattaneo, J. Vos, R. Bello, A. Palacios, S. Heuser, L. Pedrelli, M. Lucchini, C. Cirelli, F. Martin, and U. Keller, *Nat. Phys.* **14**, 733 (2018).